Magnetic Flux Measurement of Superconducting Qubits with Josephson Inductors

by

Janice C. Lee

Submitted to the Department of Electrical Engineering and Computer Science
in partial fulfillment of the requirements for the degree of

Master of Science

at the

MASSACHUSETTS INSTITUTE OF TECHNOLOGY

August 2002

Author .....
Department of Electrical Engineering and Computer Science
August 9, 2002

Certified by .....
Terry P. Orlando
Professor of Electrical Engineering
Thesis Supervisor

Accepted by .....
Arthur C. Smith
Chairman, Department Committee on Graduate Students

Magnetic Flux Measurement of Superconducting Qubits with Josephson Inductors

by

Janice C. Lee

Submitted to the Department of Electrical Engineering and Computer Science
on August 9, 2002, in partial fulfillment of the requirements for the degree of
Master of Science

Abstract

Recent research in quantum computation with superconducting qubits relies on SQUID magnetometers to distinguish the supercurrent states of the qubits. This poses a new challenge of demanding the measurement SQUID to introduce the least decoherence on the qubits during the measurement process. The SQUID is desired to operate in an unconventional way and be biased at currents significantly below the critical current level. This thesis lays the fundamental work of achieving the above by using the SQUID as a flux-sensitive inductor. The read-out relies on incorporating the SQUID inductor in a resonant circuit, and the state of the qubit is detected from the resonant frequency of the peak. A series of prototype resonant circuits were made from printed circuit boards and tested at room temperature. On-chip high-Q resonant circuits were designed to optimize the signals in the inductance measurements to about ten microvolts. Calculations of the decoherence times based on the spin-boson model were performed and the relaxation time falls in the microsecond regime.

Thesis Supervisor: Terry P. Orlando
Title: Professor of Electrical Engineering

Acknowledgments

First and foremost, I am most grateful to my supervisor, Professor Terry Orlando, for his guidance, support and insights. I thoroughly enjoyed to be part of his group and look forward to continue working with him in the future. The extra effort he puts into fostering a positive atmosphere in the group is very much appreciated. He is also an excellent and devoted teacher; I was enrolled in three of his classes all of which were wonderfully taught.

I benefit tremendously from people in my group. First, I must thank our post-doc, Dr. Ken Segall, for being enthusiastic and supportive since the very beginning of my project. He is always available for discussion, and his insights for setting the direction of the project were excellent. I also owe thanks to Donald Crankshaw for sharing his expertise in electronics and performing cryogenic experiments. He was the person who coached me through the cool-down of my first sample. I benefit a lot from him on all expects of experimental work in the group. The devices I measured were fabricated by Daniel Nakada. I am grateful to have him as a coworker and value his friendship and his generous personality.

The support from several technicians was indispensible. In particular, I would like to thank Fred Cote in the Edgerton Student Machine Shop for his infinite patience with my ambitious ideas on metal work. With his long years of experience and his collection of gadgets, my machine work has always been successful and pleasant. Thanks are also due to Terry Weir at MIT Lincoln Laboratory for giving me much-needed advice over the phone when I set up the co-ax on the new helium-4 probe, and to Daniel Adams at MTL for training me on the gold wirebonder.

I would like to acknowledge Professors Sheila Prasad and Clifton Fonstad for letting me use their network analyzer, and Dr. Daniel Oates at MIT Lincoln Laboratory for kindly taking the time to discuss RF resonant circuits with me during the early part of the project. Thanks also go to Caspar van der Wal for stopping by our group every other Tuesday to tell us stories about dilution refrigerators. I would also like to acknowledge Will Oliver with whom I had some very useful and stimulating discussions during his visits.

Richard Feynman once wrote to the mother of his student, "tell your child to stop trying to fill your head with science–for to fill your heart with love is enough!" Quite the contrary, my parents love to hear all aspects of my work with just as much enthusiasm as I do. They share my ups and downs in research, and give me excellent advice to fuel me up and keep me going. At times of discouragement, they always tell me how proud they are of my accomplishments, and remind me that "it is never easy reaching for dreams, but those who reach walk in stardust."

Contents

List of Figures

Chapter 1

Introduction

Abstract

The SQUID inductance measurement is an innovative way to detect magnetic flux signal with a SQUID magnetometer. The need to develop this new measurement scheme proves to be essential for quantum computation with superconducting qubits. It offers significant improvement over the existing switching current method in detecting the states of the Josephson persistent current qubits. This chapter begins with a description of the Josephson persistent current qubit, its two distinct energy states, and how the state of the qubit can be determined by flux measurement. The shortcoming of the existing measurement scheme will be discussed, and the improved method of using the SQUID as a magnetic-flux sensitive inductor will be proposed.

1.1 Josephson Persistent Current Qubit

Quantum computation is based on controlling the evolution of physical systems which function based on the framework of quantum mechanics. With properties only characteristic to quantum systems such as superposition and entanglement of states, quantum computers have the potential to perform some tasks exponentially faster than classical computers.

Superconducting Josephson junction circuits rank among the best systems as a candidate for realizing a quantum computer. Unlike earlier implementations involving nuclear magnetic resonance or ion traps, these superconducting systems are solid-state in nature and utilize familiar electrical devices controlled by voltages and currents. The main advantage of such an approach is that the technology for expanding one single operational qubit to a large-scale integrated computer is readily available. For quantum computation, it is important to control individual qubits as well as qubit-qubit coupling. The level of control and coupling can be more easily varied in Josephson devices for they are artificially designed and fabricated systems. However, the ease of manipulation also means the systems are coupled strongly to the outside world. This posts a challenge as qubits must also be sufficiently isolated from the environment so that they can maintain coherence throughout the computation. Extra

care must therefore be taken to reduce the source of noise and decoherence from the environment to the solid state quantum systems.

Recent research on superconducting qubits has been focused on either the charge regime (number of Cooper pairs on a superconducting island is well defined) or flux regime (phase in a superconducting loop is well defined). In particular, qubits operating in the flux regime have two distinct energy states characterized by the different magnetic flux generated in a superconducting loop. The two states can be distinguished by an extremely small difference in magnetic flux sensed by a SQUID magnetometer. One such flux-biased superconducting qubit is the Josephson persistent current qubit [1, 2]. The persistent current qubit is a single superconducting loop interrupted by three Josephson junctions in series. Upon applying an external magnetic field, a persistent current is induced in the loop as a direct consequence of fluxoid quantization, which states that the sum of the gauge-invariant phase around the loop must be an integral multiple of 2π. The presence of the three junctions gives rise to a double-well-like potential in flux space without requiring the loop to have a large geometric inductance as in the one-junction or two-junction case. This is advantageous because the smaller the size of the qubit loop, the easier it is to decouple it from environmentally induced noise.

When the external flux as seen by the qubit is biased near half integrals of a flux quantum Φ_o, the two lowest energy states correspond to persistent current circulating in opposite directions. These two current states are chosen as the logical states of the qubit. The flux of the induced current either adds or subtracts from the external flux, and by detecting the difference in the overall flux with a DC SQUID inductively coupled to the qubit, the states of the qubit can be measured. There lies the challenge of maintaining the coherence of the qubits not only throughout the computational process, but also during the period between initiating the detector and the instant at which the final results are accurately measured and stored. In particular, the detector should not introduce enough noise to cause the qubit to transfer from the original state to another during the measurement process.

Quantum superposition of the two qubit states have been verified experimentally by pulsed microwave spectroscopy [3]. As predicted by theory, the energy separation between the ground state and the first excited state was evidenced at the anti-crossing in flux space ($0.5\Phi_o$) where the two uncoupled persistent-current states would have been degenerate.

1.2 The Switching Current Measurement and its Drawbacks

The choice of a good measurement setup to detect the qubit states is of paramount importance in reducing environmentally induced decoherence. The process of design-

ing a good detector presents us with the usual quantum mechanics dilemma. For a detector that is only weakly coupled to the qubit, its backaction on the qubit is small. However, the measured signal can be too weak to be resolved by the measurement apparatus. On the other hand, a strong coupling between the detector and the qubit yields a strong signal but also introduces severe backaction and decoherence on the qubit.

The additional flux generated by the persistent current in the qubit can be sensed by a SQUID magnetometer. The size of the qubit flux as seen by the SQUID depends on the strength of the coupling. The coupling in turn depends on the mutual inductance M between the qubit and the SQUID, and the size of the persistent current I_P within the qubit loop. The resultant flux due to the persistent current sensed by the SQUID is between $0.001\Phi_o$ to $0.01\Phi_o$. Therefore, the two qubit states can be distinguished by a difference in flux signal of $0.002\Phi_o$ to $0.02\Phi_o$. The present detection scheme employs a non-shunted (underdamped) DC SQUID and uses the property that its critical current is a function of magnetic flux. In principle, SQUIDs have a typical sensitivity of $10^{-5}\Phi_o/\sqrt{Hz}$ and should be able to detect this minute qubit signal. One of the ways to directly measure the critical current is the so-called switching current method. Typically, one ramps the current through the SQUID and determines the discontinuous point at which the junction switches from the superconducting state to the finite voltage state.

The switching current method has some major disadvantages. Firstly, one is most concerned about the decoherence of the qubit introduced by the switching DC SQUID. Calculations based on the spin-boson model have showed that the level of decoherence increases with the amount of bias current that is passed through the SQUID ([4] pg.55-66). In particular, the relaxation and dephasing times decrease drastically as the bias current approaches the critical current. However, the switching current method relies on the discontinuous action, and by definition cannot avoid the high bias regime. The backaction of the measurement process can thus severely interfere with the original state of the qubit.

Secondly, the switching action of the SQUID to the finite voltage state excites a large number of quasi-particles, which must then be allowed to relax to the superconducting state before another measurement can be performed. This relaxation time can be fairly long and may restrict the repetition rate of the measurements [5].

Thirdly, the choice of an underdamped DC-SQUID has some drawbacks. Due to thermal fluctuations and other sources of noise, the switching current is suppressed and is lower than the actual critical current. The measured switching currents are usually distributed over a finite current range and are plotted in a switching current histogram. The uncertainty corresponds to the width of the histogram. This uncertainty can be larger than the qubit flux signal, and thus it may be necessary to measure the signal based on averaging over 1000 to 10000 switching events.

Finally, the switching current method is not very efficient. Over a cycle of the hysteretic I-V curve, the switching event only takes up a small fraction of the time. During the waiting time before readouts, there is a possibility for the qubit to tunnel from the original state to another. In other words, the time required to perform a switching current measurement has to be much shorter than the mixing rate (inversely proportional to the relaxation time) of the qubit. However, the upper bound of the measurement rate is limited by an order lower than the filter bandwidth [4].

While seeking for alternatives, one may consider a damped DC SQUID. It is the most common way by which a SQUID magnetometer is operated. However, the damped DC SQUID requires one to bias the current above the critical current, which may even be more catastrophic in terms of the level of decoherence. Moreover, the voltage-SQUID has a non-hysteretic I-V characteristic which requires the junctions to be shunted with resistors. The shot noise introduced by the resistive shunt unfortunately causes yet additional decoherence on the qubit even when no measurement is performed. This problem can be improved if the SQUID is placed very far away from the qubit [6]. However, this is not desired for the three-junction qubit due to its minute flux signal.

Conventional ways to operate DC SQUID magnetometers such as using it as a switching current detector or biasing it in the finite voltage state are not the best candidates to be used for quantum computation with superconducting Josephson qubits. An original and innovative method has to be developed with factors such as shot noise, decoherence time, and short measurement time taken into account. These are the motivation and ultimate goal of the SQUID Inductance Measurement scheme.

1.3 The SQUID Inductance Measurement

The above disadvantages of the present measuring scheme posts a need to operate the SQUID magnetometer differently. The manner of which the level of decoherence is related to the size of the bias current suggests that the backaction of the measuring SQUID can be strongly reduced at low bias current. This is possible with the Inductance Measurement Method originally proposed in [7]. The basic principle is to use the SQUID as a flux-sensitive inductor. In other words, the Josephson inductance across the junctions of a DC SQUID is a periodic function of the magnetic flux which threads the loop. Such an operation mode requires the SQUID biased only at low current along the supercurrent branch, and the qubit signal can be detected without any discontinuous actions. The read-out can be performed by inserting the SQUID inductor in a resonant circuit, and the state of the qubit is detected from the position of the resonant peak.

1.4 Overview of Thesis

This thesis studies the SQUID inductance measurement scheme and lays the experimental framework for implementing the idea. Chapter 2 begins with a derivation of the Josephson inductance of a SQUID, and how it can be used as a flux-sensitive inductor. The principles of the inductance measurement will also be outlined. A series of prototype resonant circuits were made from chip components on printed circuit boards, and the results from the room-temperature testing will be presented in chapter 3. Chapter 4 presents the design of four high-Q on-chip circuits optimized for the inductance measurement. The optimal operating points will be proposed, and the expected signal due to the qubit will be calculated. Finally, the decoherence calculations based on the spin-boson model will be presented in chapter 5.

Chapter 2

Principles of SQUID Inductance Measurement

Abstract

This chapter begins with the derivation of the inductance across a single Josephson junction. The derivation is then extended to the case of a DC SQUID. The non-linear effects of the Josephson inductance will also be discussed. It will be shown that the SQUID is a flux and bias-current sensitive inductor. Subsequently, the principles of measuring the Josephson inductance by incorporating it in a LC resonant circuit will be introduced.

2.1 Inductance of Josephson junctions

2.1.1 Inductance of a single Josephson junction

In the circuit definition, the inductance across an element is defined as

$$V(t) = L\frac{dI(t)}{dt} \tag{2.1}$$

One can regard the inductance L as a measure of how fast the current passing through the element has to change to produce a certain voltage. While typical circuit elements have an inductance L that is constant with time and operating conditions, we will relax this restriction here and allow the inductance to vary with time. As will be seen later, the *parametric inductance* L(t) as defined in eqn. 2.2 can better describe the Josephson inductance that is non-linear and usually time-varying during operation. It is useful to compare this with the case of a varacter diode, where the *parametric capacitance* is also a time-varying parameter that depends on the operating bias voltage.

$$V(t) = L(t)\frac{dI(t)}{dt} \tag{2.2}$$

We will now consider a single Josephson junction as a circuit element. The current passing through the junction is related to the invariant phase according to the current-phase relation:

$$I(t) = I_{CO} \sin \varphi(t) \tag{2.3}$$

where I_{CO} is the critical current and I(t) is the bias current through the junction. The voltage across the junction is given by the voltage-phase relation:

$$V(t) = \frac{\Phi_o}{2\pi} \frac{d\varphi(t)}{dt} \tag{2.4}$$

We know that when the Josephson junction is voltage-biased, an ac current is developed and this is known as the AC Josephson effect. More thought would actually lead to the observation that the junction is actually inductive. Since a superconducting Josephson junction has zero resistance, the voltage has to be distributed across some purely reactive impedance. The voltage-phase relation tells us that the voltage manifests itself as a rate of change of phase. The phase in turn is related to the current in a non-linear fashion. Thus, the voltage is somehow related to the rate of change of current, which is exactly the definition of an inductive element (eqn. 2.2).

Mathematically, we can derive the expression of the non-linear Josephson inductance L_{JO} from eqn. 2.3 and eqn. 2.4. First, assume we are passing through the junction a current I(t) which has both AC and DC components as in fig. 2-1.

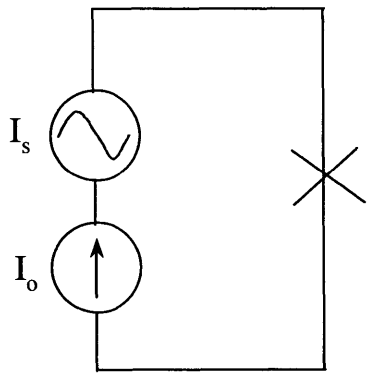

Figure 2-1: Circuit setup for deriving Josephson inductance. The cross represents a pure Josephson junction as a circuit element. I_O is the DC offset and I_S is the AC oscillation.

We take the time derivative of eqn. 2.3 and obtain:

$$\frac{dI}{dt} = I_{CO} \cos \varphi(t) \frac{d\varphi}{dt} \tag{2.5}$$

But $\frac{d\varphi}{dt}$ can be expressed in terms of voltage by rearranging eqn. 2.4 to obtain:

$$\frac{dI}{dt} = I_{CO}\cos\varphi(t)(\frac{2\pi V(t)}{\Phi_o}) \tag{2.6}$$

By comparing eqn. 2.6 with the definition of inductance given in eqn. 2.2, one could extract the Josephson inductance as

$$L_{JO} = \frac{\Phi_o}{2\pi I_{CO}\cos\varphi(t)} \tag{2.7}$$

For the special case when (1) the AC oscillation is small compared to the DC offset ($I_S \ll I_O$), and (2) the total I(t) is along the supercurrent branch, then $\sin\varphi \approx \frac{I_O}{I_{CO}}$ and is approximately constant. By using the identity $\cos\varphi = \sqrt{1-\sin^2\varphi}$, the expression for L_{JO} is obtained as eqn. 2.8 and plotted in fig. 2-2.

$$L_{JO} = \frac{\Phi_o}{2\pi I_{CO}\sqrt{1-(\frac{I_O}{I_{Co}})^2}} \tag{2.8}$$

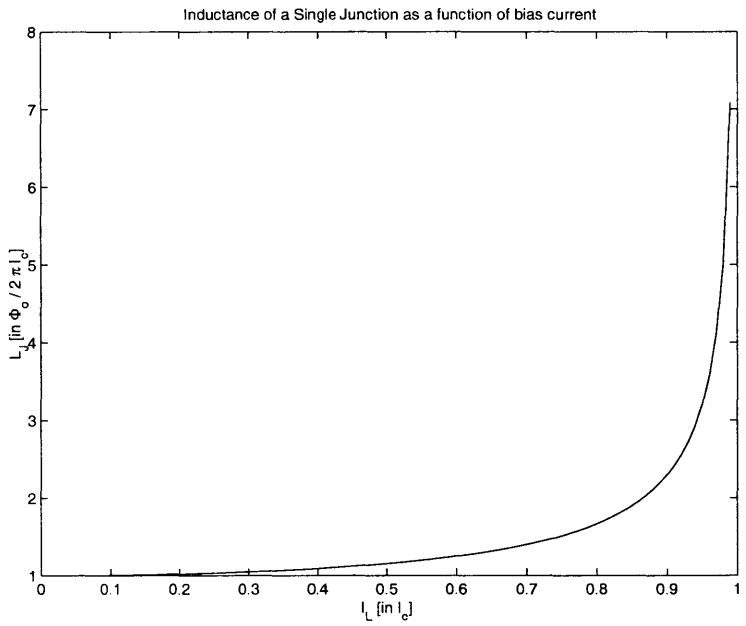

Figure 2-2: Inductance of a single Josephson junction as a function of bias current I(t). Assume $I_S \ll I_O$

Eqn. 2.7 was obtained by defining a parametric inductance in eqn. 2.2. This is a common approach widely used in circuit analysis. Alternatively, one can rigorously treat the voltage as the negative rate of change of the magnetic flux, which in turn is equal to the product of L(t) and I(t) as shown in eqn. 2.9. Note that the negative sign is omitted for simplicity as it can be easily absorbed in the other parameters. With this approach, the Josephson inductance can be derived as follows:

$$V(t) = \frac{d(L(t)I(t))}{dt} \tag{2.9}$$

By the product rule, we obtain

$$V(t) = L(t)\frac{dI(t)}{dt} + I(t)\frac{dL(t)}{dt} \tag{2.10}$$

Note that the first term is the same as eqn. 2.2 and the second term is now additional. We will go ahead and find the expression for L_{JO} from the definition in eqn. 2.9 where it is treated rigorously as time-dependent. First, rewrite the voltage-phase relation 2.4 as

$$V(t) = \frac{\Phi_o}{2\pi}\frac{d(\varphi(t))}{dt} = \frac{d}{dt}\left(\frac{\Phi_o\varphi(t)}{2\pi I(t)}I(t)\right) \tag{2.11}$$

and we extract L_{JO} based on eqn. 2.9:

$$L_{JO} = \frac{\Phi_o\varphi(t)}{2\pi I_{CO}\sin\varphi(t)} \tag{2.12}$$

Again, if $I_S \ll I_O$, L_{JO} can be expressed in a more useful form:

$$L_{JO} = \frac{\Phi_o \arcsin(\frac{I}{I_{CO}})}{2\pi I_{CO}\sqrt{1-(\frac{I}{I_{CO}})^2}} \tag{2.13}$$

Eqns. 2.8 and 2.13 are plotted in fig. 2-3. It can be seen that the time-dependent definition yields a smaller inductance, but the difference is significant only for large current values. Since the SQUID inductance measurement will be biased only at low current values, both methods are comparable in that regime. Since eqn. 2.7 is more commonly used, it will be adopted for the rest of the thesis.

2.1.2 Inductance of a DC SQUID

The above derivation of the Josephson inductance can be extended for the case of a DC SQUID. Fig. 2-4 shows a DC SQUID made up of two identical junctions each with I_{CO}. The overall critical current I_C of the SQUID depends both on I_{CO} and the magnetic flux Φ which threads the loop:

$$I_{C,sq} = I_C\cos\frac{\pi\Phi}{\Phi_o} \tag{2.14}$$

where $I_C = 2I_{CO}$. Thus the Josephson inductance of a SQUID is given by:

$$L_{J,sq}(\Phi, I_{sq}) = \frac{\Phi_o}{2\pi I_C|\cos\frac{\pi\Phi}{\Phi_o}|\sqrt{1-(\frac{I_{sq}}{I_C\cos\frac{\pi\Phi}{\Phi_o}})^2}} \tag{2.15}$$

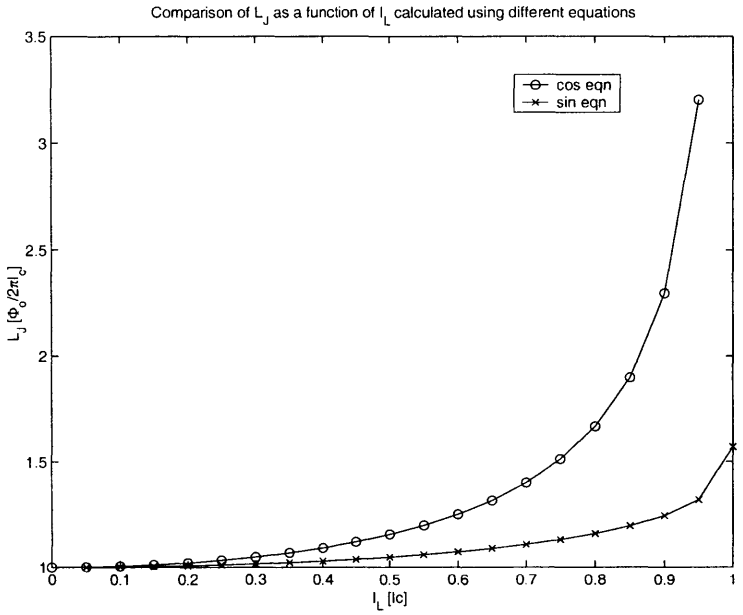

Figure 2-3: Comparison of L_J as derived from the two definitions mentioned above. The difference is not significant in the inductance measurement regime.

The dependence of $L_{J,sq}$ on I_{sq} and Φ is illustrated more clearly in the plots 2-5 and 2-6. Note that the inductance is normalized to units of $[\frac{\Phi_o}{2\pi I_C}]$.

Therefore a SQUID is effectively a bias-current and flux-dependent inductor. It is important to realize that the Josephson inductance originates from the junctions, and is an effect *in addition to* the SQUID loop inductance which depends only on the geometry and does not vary with biasing conditions.

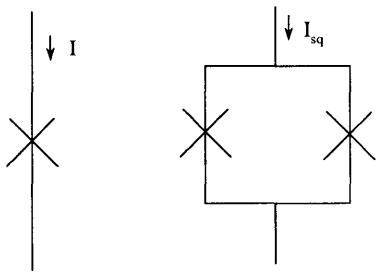

Figure 2-4: Single junction (left) and a DC SQUID (right)

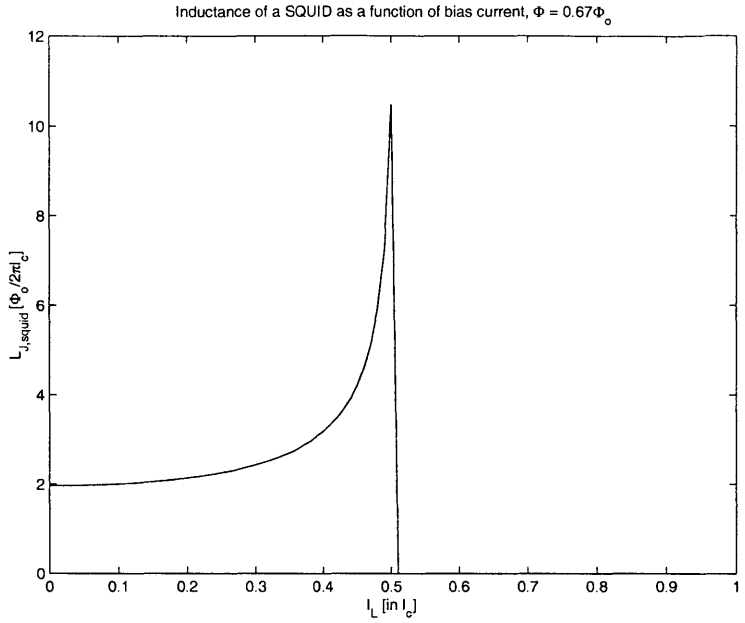

Figure 2-5: SQUID Josephson inductance as a function of bias current, with $\Phi = 0.67\Phi_o$. The actual switching current is suppressed to $I_c \cos\frac{\pi\Phi}{\Phi_o}$, above which the SQUID is no longer in the supercurrent branch and the inductance becomes complex. For $\Phi = 0$, the SQUID inductance reduces to a single junction case (fig. 2-2).

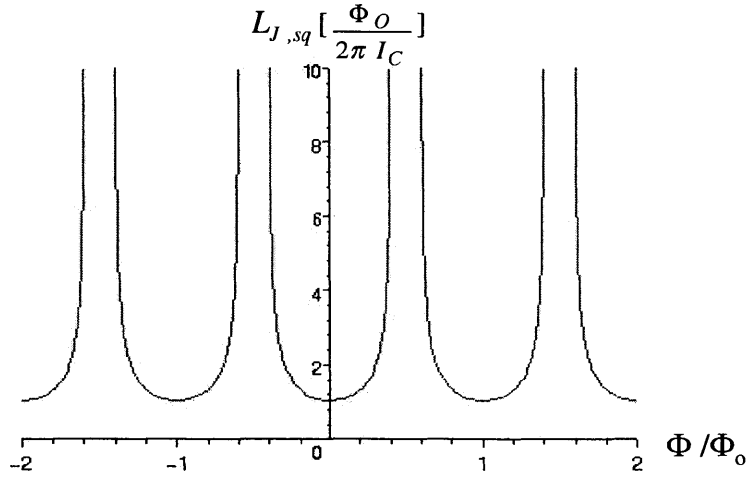

Figure 2-6: SQUID Josephson inductance as a function of flux through the loop.

2.1.3 DC SQUID Parameters from Lincoln Lab Fabrication Process

It is useful at this point to get a sense of the size of the DC SQUID Josephson inductance fabricated in the Lincoln Laboratory process. At the bias point of zero magnetic field and $\frac{I_{sq}}{I_C} = 0.3$, the SQUID inductance L_J is about 0.1 to 0.5nH (for I_C between 0.7 to 4.8μA). If the field bias is raised to $0.67\Phi_o$, L_J is about 0.2 to 1.1nH. How these values are obtained will be more clear in the later part of the thesis. It is sufficient to realize at this point that the Josephson inductance are on the order of nanohenries.

2.2 Resonance Measurement of SQUID Josephson Inductance

2.2.1 RLC Resonance

We have shown that the SQUID Josephson inductance varies according to the qubit flux signal that it senses. The next stage is to develop a scheme to measure the inductance effectively. The method to measure the SQUID inductance proposed in [7] is to incorporate the SQUID in a RLC resonant circuit. The resonant frequency of the circuit depends on the inductance of the circuit. Upon the addition of the qubit signal, the corresponding change in the SQUID inductance can be measured by keeping track of the peak position. For illustrative purposes, a simple parallel RLC resonant circuit is shown in fig. 2-7. The actual inductance measurement circuit will be more complex than this, but the principles are the same. The parallel configuration is chosen over its series counterpart, because one can show that the series case is easily overdamped unless the resistance R is very small. In the diagram, the SQUID is shown as an ordinary inductor, and the resistance R includes the 50Ω source and amplifier impedances connected to it. The circuit is fed by a DC current source and a single frequency AC source.

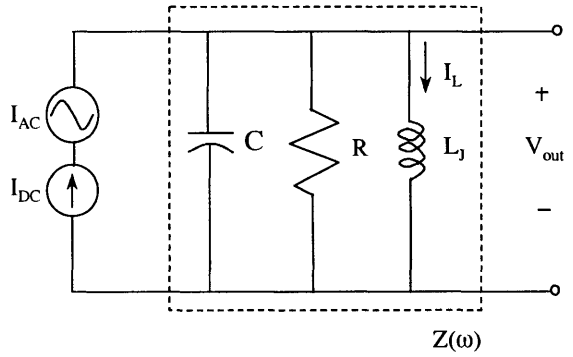

Figure 2-7: Parallel RLC resonant circuit for inductance measurement

The frequency-dependent impedance $Z(\omega)$ of the network with output taken across the resistance R is given by:

$$|Z(\omega)| = \frac{1}{\sqrt{R^2 + [\omega L - (\frac{1}{\omega C})]^2}} = \frac{R(\frac{\omega\omega_o}{Q})}{\sqrt{(\omega_o{}^2 - \omega^2)^2 + (\frac{\omega\omega_o}{Q})^2}} \tag{2.16}$$

where ω_o is the resonant frequency given by

$$\omega_o = \frac{1}{\sqrt{LC}} \tag{2.17}$$

and Q is the quality factor which measures the sharpness of the resonant peak. Q is equal to the ratio of the effective resistance to the reactance of the inductor X_L at ω_o. (Note that X_L equals X_C at resonance, where $X_L = \omega L$ and $X_C = \frac{1}{\omega C}$)

$$Q = \frac{R}{\omega_o L} = \omega_o RC \tag{2.18}$$

This above analysis for RLC resonant circuits assumes the circuit elements to be linear with constant values of R, L and C. For the inductance measurement circuit, only the values of R and C are constant and satisfy the above condition, but the SQUID inductance varies in a *non-linear fashion* with the size of the bias current, which in turn oscillates with time. In the limit of small amplitude of the AC oscillation, the SQUID inductance is fairly constant with time, and one can treat the SQUID as a lumped-element inductor with inductance given by eqn. 2.15. However if the amplitude of the oscillation is comparable to the DC bias, the SQUID inductance varies significantly at the same rate as the driving frequency. To completely describe the dynamics of such a resonant circuit requires solving the non-linear second-order differential equation for circuit 2-7:

$$\begin{aligned} I_O + I_S\cos(\omega t) &= I_c\sin(\varphi(t)) + \frac{V(t)}{R} + C\frac{dV}{dt} \\ &= I_c\sin(\varphi(t)) + \frac{\Phi_o}{2\pi}(\frac{1}{R})\frac{d\varphi}{dt} + \frac{\Phi_o}{2\pi}(C)\frac{d^2\varphi}{dt^2} \end{aligned} \tag{2.19}$$

The differential equation is second order in $\varphi(t)$ which is the gauge invariant phase. To calculate the transfer characteristics for a range of frequency, one has to solve the equation for $\varphi(t)$, $\frac{d\varphi}{dt}$, and hence V(t) at each frequency, and subsequently calculate the instantaneous impedance $Z(t) = \frac{V(t)}{I(t)}$. Such an analysis was carried out on a circuit similar to fig. 2-7 [8], and the resulted resonant peak is slightly asymmetric with the maximum point leaning towards the low-frequency side. The peak has a sharper slope on the low-frequency side as well. Considering that the actual inductance measurement circuit is too complex for the differential equation approach to be feasible, we will assume the actual resonant peak to have a similar deformation as in the simple case, and the effect will not affect the principles of the operation scheme. For the rest of the thesis, we will proceed with a *quasi-static approach* and assume

the SQUID as a lumped inductor with L_J given by:

$$L_J = \frac{\Phi_o}{2\pi I_c |\cos(\pi\frac{\Phi}{\Phi_o})|\sqrt{1-\frac{(I_{dc}+I_{ac})^2}{I_c^2 cos^2(\pi\frac{\Phi}{\Phi_o})}}} \tag{2.20}$$

This is similar to eqn. 2.15 except that I_{sq} is now replaced by I_{dc} and I_{ac}.

Returning to eqn. 2.17, we can see that a change in SQUID inductance upon the qubit flux signal will be indicated by a change in resonant frequency. This is the basis of how the flux signal can be detected. The operating procedures will be briefly outlined below. They will be revisited in more details in chapter 4 with calculations using the actual circuit parameters.

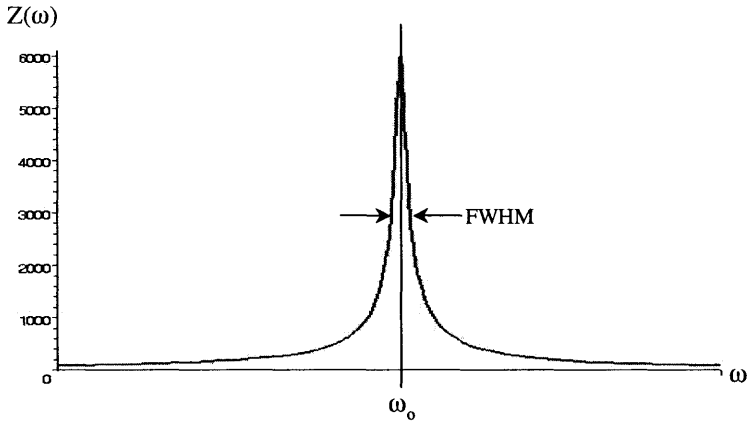

Figure 2-8: Re [Z] as a function of frequency

2.2.2 Operating Conditions for the SQUID

DC Current Bias

Recall that the SQUID inductance L_J depends both on the bias current and the flux. We will begin by first focusing on the effect of the bias current and assume the flux is kept constant for now. The SQUID is to be operated at a DC bias current of $0.3I_C$. The DC offset is chosen for two reasons: (1) it is significantly away from the critical current; the level of decoherence introduced to the qubit can be kept low. (2) With reference to fig. 2-2, we can see that at this DC offset, the inductance varies linearly with the current. Thus any additional non-linear effect due to the AC oscillation can be minimized. To bias the SQUID at the right DC level, one can simply apply a DC current source to the overall resonant circuit. Since the SQUID is biased along the supercurrent branch ($0.3I_C \ll I_C$), all of the DC current will pass through

the SQUID branch.

AC Current Bias

In addition to the DC offset, an AC oscillating current of amplitude $0.1I_C$ and frequency about 500MHz is superimposed on the SQUID. The amplitude affects the size of the output signal, and will be discussed in further details in chapter 4. The frequency is chosen to be near 500MHz so that it is significantly away from the frequency range of 5-15GHz, over which the signal is sensitive to the qubit and can cause unwanted excitations.

Over an AC cycle, the value of L_J oscillates about the DC offset point. As a result, the resonant peak of the circuit also oscillates accordingly. This shift in peak position due to the AC variation is a side-effect, and should be distinguished from the shift due to the flux signal. Fortunately, this can be achieved because the shift due to the AC variation varies over a cycle, while the shift due to the flux is independent of time. The AC effect will be approximated by taking the time-average of the peak positions over a cycle to give a resultant peak which has a broader FWHM (fig. 2-9). The flux signature will be an additional shift in the position of the *broadened* peak.

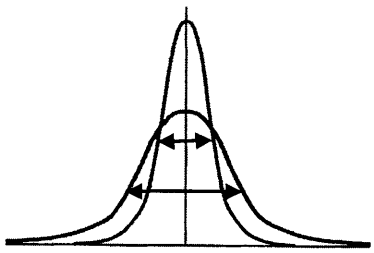

Figure 2-9: Broadening of peak due to the AC effect

2.2.3 Measuring the Inductance Change as a Voltage signal

On the preliminary level, one may suggest observing the shift in peak position by measuring the transfer function with a network analyzer at the two flux values. However, this approach does not allow us to keep the current bias through the SQUID at a certain level over the whole frequency range. This will be explained in further details in chapter 4. For now, it is enough to note that the measurement is done at a single frequency, and the shift in peak position can be mapped to a voltage signal as follows. The voltage across the output resistance of the resonant circuit is given by

$$V_{\omega_b} = I_{\omega_b} \times Z(\omega_b) \tag{2.21}$$

where ω_b is the bias frequency. Upon a change in magnetic field, the peak position shifts to a new ω_o. Since our current frequency remains biased at ω_b, we will sense a voltage difference across the output given by

$$\Delta V_{\omega_b} = I_{\omega_b} \times \Delta Z(\omega_b) \tag{2.22}$$

This is illustrated in fig. 2-10. $\Delta Z(\omega_b)$ is maximum if ω_b is close to ω_o, where $Z(\omega)$ has the sharpest slope. This establishes an additional constraint that ω_b has to be near ω_o.

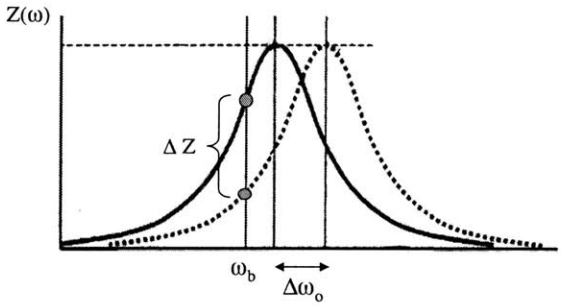

Figure 2-10: Shift in peak position upon a change in magnetic field. ΔZ is to be detected as a voltage signal

2.2.4 Summary

This chapter laid the foundation for understanding the basic ideas behind the SQUID inductance measurement. We have taken a rather qualitative approach. In chapter 4, the measurement procedures will be revisited and explained more thoroughly based on some specific circuit designs. Calculations with the actual parameters will then be presented.

Chapter 3

Room-temperature Measurements of Resonant Circuits

Abstract

Prototype resonant circuits were built from surface mount components on printed circuit boards. The first part of this chapter covers the experimental aspects of the making of the printed circuit boards such as choosing the suitable surface mount components, understanding the circuit parasitics, and designing the co-planar waveguide structures. The second part presents the results from the reflection and transmission measurements of the resonant circuits with a network analyzer at room temperature. The value of the parasitics in the measured circuits were estimated and confirmed with PSPICE simulations. A resonant circuit with improved characteristics was designed with RF techniques to optimize the conditions for the inductance measurement, and was also tested to work at room temperature. Finally, the experimental set-up for RF measurements at 4 kelvin will be presented.

3.1 Making Resonant Circuits on Printed Circuit Boards

The resonant circuits for the SQUID inductance measurements were implemented with printed circuit boards. The idea was to replace the SQUID with a surface mount inductor of comparable inductance, and to build the rest of the resonant circuit with surface mount capacitors and resistors as well. This allows one to effectively implement and test the resonant circuit designs, and to measure their reflection and transmission characteristics with a network analyzer at room temperature.

3.1.1 Surface Mount Components

When one moves from DC to RF (radio frequency) measurements, the stray reactances (parasitics) due to the leads and bulk materials of the circuit elements start to dominate. In addition, for lumped-element analysis to hold, one has to ensure

the dimension of the circuit elements be much smaller than the wavelength of the signal. For these purposes, surface mount (chip) components are used to build RF circuits. Their performance is better than the leaded components due to the compact size. Nevertheless, the parasitics of the chip components cannot be totally ignored and may still come into effect in the measurements. Figure 3-1 shows the equivalent circuit and the impedance characteristic of a real inductor [9].

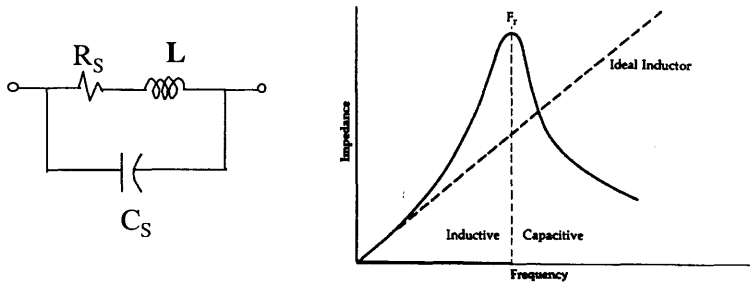

Figure 3-1: Equivalent circuit (left) and the impedance characteristic (right) of a real surface mount inductor [9].

In the circuit model, L represents the ideal inductance, C_S is the capacitance between adjacent windings of the inductor coil, and R_S is the resistance distributed across the coil. It is convenient to define the reactance of the inductor as $X_L = \omega L$, then the Q of the inductor is given by $\frac{X_L}{R_S}$ and is desired to be as high as possible at the frequencies of interest. The presence of the stray capacitance C_S causes the impedance X_L to deviate from the ideal linear characteristic and instead peak at the so-called self-resonant frequency at which L and C_S resonate. The self-resonant frequency is given by $F_S = \frac{1}{2\pi\sqrt{LC_S}}$ and is desired to be much higher than the frequencies of interest.

Figure 3-2 shows the equivalent circuit and the impedance characteristics of a chip capacitor. The Q of the capacitor is given by $\frac{X_C}{ESR}$, where X_C is the reactance of the capacitor given by $\frac{1}{\omega C}$. ESR stands for Effective Series Resistance and is the effective resistance of R_S and R_P. The maximum absorption peak occurs at $F_S = \frac{1}{2\pi\sqrt{L_S C}}$. It turns out that the parasitics of the chip capacitors were much more dominant in our measurements than those of the inductors. This is because the inductance values needed for the experiment is only on the order of nanohenries. On the other hand, the required capacitance values are fairly large (10-100pF) especially for typical RF measurements. Larger-value components tend to exhibit more internal stray than smaller-value ones.

3.1.2 Co-Planar Waveguides

To have better control of the parasitics of the circuit, and to match the characteristic impedance of the trace on the circuit board to the 50Ω coaxial cables, co-planar

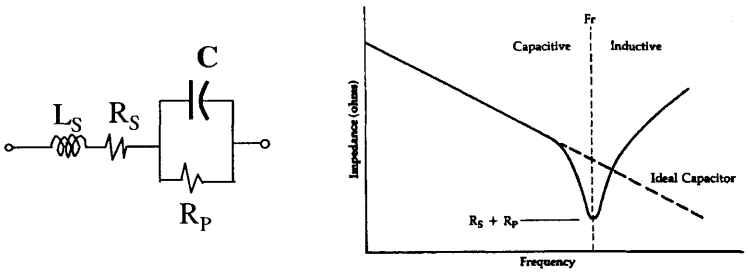

Figure 3-2: Equivalent circuit (left) and the impedance characteristic (right) of a surface mount capacitor [9].

waveguides were placed on the printed circuit boards. The schematic of a co-planar waveguide is shown in fig. 3-3. This particular waveguide structure was chosen because the center conductor and the two ground planes reside on the same plane. As a result, the surface mount components can be mounted in series or shunt configuration very easily. It also eliminates the need for drilling hole vias and makes fabrication simpler. In addition, the properties of a co-planar waveguide only depend on the relative dimensions of the center conductor, the gap, and the thickness, and thus the waveguide can be scaled as desired and still have the same properties.

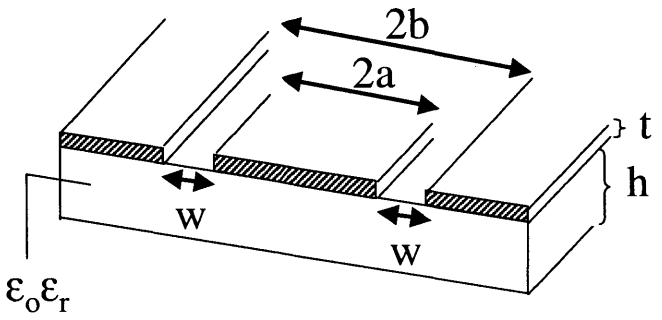

Figure 3-3: Schematic of a coplanar waveguide on a dieletric substrate of finite thickness. [10]

We are mostly interested in calculating the effective dielectric constant (ϵ_{eff}), the characteristic impedance (Z_o), and the stray inductance of the line. The closed form expressions are obtained using the conformal mapping techniques [10] and are given below:

$$\epsilon_{eff} = 1 + \frac{(\epsilon_r - 1)}{2} \frac{K(k')K(k_1)}{K(k)K(k_1')} \tag{3.1}$$

$$Z_o = \frac{30\pi}{\sqrt{\epsilon_{eff}}} \frac{K(k')}{K(k)} \tag{3.2}$$

$$L = \frac{\mu_o}{4}\frac{K(k')}{K(k)} \tag{3.3}$$

where K(x) is the complete elliptic integral of the first kind, with modulus x given by:

$$k = \frac{a}{b} \tag{3.4}$$

$$k_1 = \frac{\sinh(\frac{\pi a}{2h})}{\sinh(\frac{\pi b}{2h})} \tag{3.5}$$

$$k' = \sqrt{1-k^2} \tag{3.6}$$

$$k_1' = \sqrt{1-{k_1}^2} \tag{3.7}$$

3.2 Resonant Measurements with Network Analyzer

3.2.1 Scattering Matrix Parameters

We characterize the resonant circuits by measuring the scattering parameters with a vector network analyzer. The scattering parameters relate the voltage waves incident on the ports to those reflected from the ports, and *completely* describe the network. Fig. 3-4 shows a general two-port network with voltage waves indicated [11].

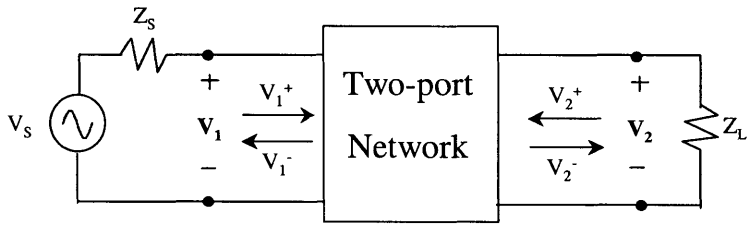

Figure 3-4: A general two-port network with arbitrary source and load impedances.

The scattering matrix is defined as

$$\begin{bmatrix} V_1^- \\ V_2^- \end{bmatrix} = \begin{bmatrix} S_{11} & S_{12} \\ S_{21} & S_{22} \end{bmatrix} \begin{bmatrix} V_1^+ \\ V_2^+ \end{bmatrix} \tag{3.8}$$

which can be expanded as

$$V_1^- = S_{11}V_1^+ + S_{12}V_2^+ \tag{3.9}$$

$$V_2^- = S_{21}V_1^+ + S_{22}V_2^+ \tag{3.10}$$

The scattering parameters are defined by the ratio of the voltage waves and are individually given by:

$$S_{11} = \frac{V_1^-}{V_1^+}\,|_{V_2^+=0} \tag{3.11}$$

$$S_{21} = \frac{V_2^-}{V_1^+}\,|_{V_2^+=0} \tag{3.12}$$

$$S_{12} = \frac{V_1^-}{V_2^+}\,|_{V_1^+=0} \tag{3.13}$$

$$S_{22} = \frac{V_2^-}{V_2^+}\,|_{V_1^+=0} \tag{3.14}$$

Now, we will focus on the parallel LC resonant circuit as a two-port network. We consider the specific case where the resonant circuit is terminated by 50Ω cables at both ends as in the actual measurements. The simplified network is shown in fig. 3-5. Our goal is to measure the transfer function of the circuit $\frac{V_{out}}{V_{in}}(\omega)$. We will see how this can be extracted from the S-parameter measurements. Because of the symmetry of the circuit, we only have to focus on two of the S-parameters S_{11} (same as S_{22}) and S_{21} (same as S_{12}).

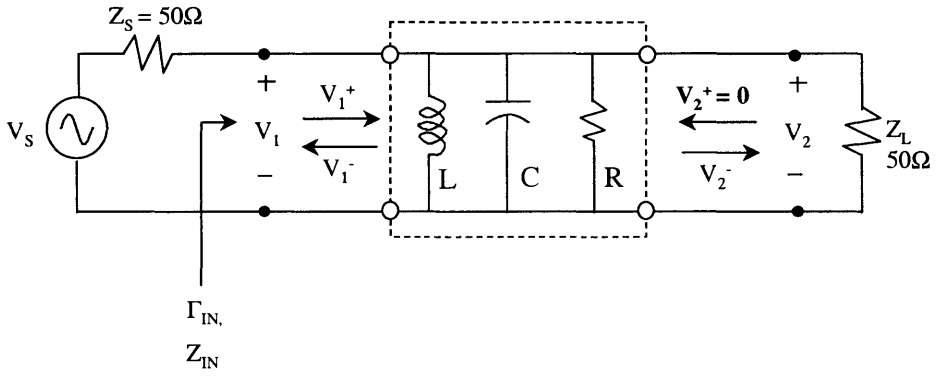

Figure 3-5: A parallel RLC circuit as a two-port network. For our measurements, both ports are always terminated with 50Ω cables.

For a matched load ($Z_L = 50$), V_2^+ is always zero, and the expressions for V_1^- and V_2^- reduce to:

$$V_1^- = S_{11}V_1^+ \tag{3.15}$$

$$V_2^- = S_{21} V_1^+ \tag{3.16}$$

It is useful to find the reflection coefficient Γ_{in} looking into the network from the source. By definition,

$$\Gamma_{in} = \frac{V_1^-}{V_1^+} \tag{3.17}$$

This can be expressed in terms of the impedances of the network based on transmission line theory [11]:

$$\Gamma_{in} = \frac{Z_{in} - Z_o}{Z_{in} + Z_o} \tag{3.18}$$

Since the input impedance Z_{in} looking into port 1 is given by the parallel combination of $Z_R//Z_C//Z_{inductor}//Z_L$, we can obtain an expression for Γ_{in}:

$$\begin{aligned} \Gamma_{in} &= \frac{Z_{in} - Z_o}{Z_{in} + Z_o} \\ &= \frac{(Z_R//Z_C//Z_{inductor}//50) - 50}{(Z_R//Z_C//Z_{inductor}//50) + 50} \end{aligned} \tag{3.19}$$

The definition of S_{11} (eqn. 3.11) is almost the same as Γ_{in} (eqn. 3.17), except that S_{11} has an additional condition that V_2^+ must be zero. This simply means that port 2 has to be terminated in a 50Ω matched load and there is no back-reflection into the network. When we calculated Γ_{in} above for our particular measurement setup, we already assumed the load is matched, and thus S_{11} is conveniently given by eqn. 3.19. It is useful to keep in mind that whenever port 2 is terminated by a matched load, $S_{11} = \Gamma_{in}$.

$$S_{11} = \Gamma_{in}|_{Z_L=50} \tag{3.20}$$

We will now study the forward transmission property of the two-port by finding the ratio of the voltages at the input port and the output port, i.e. $\frac{V_2}{V_1}$, where V_1 and V_2 are defined in figure 3-5. By definition,

$$V_1 = V_1^- + V_1^+ \tag{3.21}$$

$$V_2 = V_2^- + V_2^+ = V_2^- \tag{3.22}$$

The transfer characteristics in terms of the S-parameters can be derived as follows:

$$\begin{aligned}\frac{V_2}{V_1} &= \frac{V_2^-}{V_1^+ + V_1^-} \\ &= \frac{\frac{V_2^-}{V_1^+}}{1 + \frac{V_1^-}{V_1^+}}|_{V_2^+=0} \\ &= \frac{S_{21}}{1 + S_{11}}\end{aligned} \tag{3.23}$$

It is interesting to note that the transfer characteristics $\frac{V_2}{V_1}$ defined right at the ports depends not only on the transmission parameter S_{21} but also on the reflection parameter S_{11}. This is because only part of the source voltage V_s is absorbed into the network. The input voltage at the port is given by the voltage divider in equation 3.24. It should also be mentioned that the standard voltage divider holds for our circuit analysis because over the frequency range of interest, the wavelength is much longer than the circuit dimension.

$$V_1 = V_s \frac{Z_{in}}{Z_s + Z_{in}} \tag{3.24}$$

Although we can learn about the transfer property by finding $\frac{V_2}{V_1}$ as above, the concern about back-reflection can be avoided if we view the voltage source as part of the "network" as well. There is no reflected voltage right at the source because Z_s is matched. It is therefore convenient to define the transfer function of the RLC resonant circuit as the ratio between the *output voltage to the source voltage* $\frac{V_{out}}{V_s}$, instead of the ratio between the *voltages at the ports* $\frac{V_2}{V_1}$. In fact the former is more consistent with the conventional definition of the transfer function of a resonant circuit. Given the matched source and load impedances, V_s is equal to V_1^+ and V_{out} is equal to V_2^-. Thus $\frac{V_{out}}{V_s}$ is simply given by S_{21}. We will adopt this convention and include the source as part of network when we analyze the measurement results, and S_{21} will be the direct measurement of the transfer function of the resonant circuit $\frac{V_{out}}{V_s}$ as long as port 2 is terminated with a matched load.

$$S_{21} = \frac{V_2^-}{V_1^+}|_{V_2^+=0} = \frac{V_{out}}{V_s} \tag{3.25}$$

3.2.2 Experimental Data

Simple LC resonant circuits were built on printed circuit boards, and the S_{11} and S_{21} characteristics were measured with the network analyzer HP 8510B. The effective resistance R of the LC resonant circuits in fig. 2-7 is mainly dominated by the parallel combination of the 50Ω source and load impedances. Since the Q of

the peak is directly proportional to R, it is desired to raise the Q by raising the effective resistance R as seen by the circuit. However, simply inserting a large shunting resistance in parallel with the LC circuit cannot achieve the purpose, as $R_{eff} = R_s//R_L//R_{shunt} \approx R_s//R_L = 50\Omega//50\Omega$, assuming $R_{shunt} \gg 50\Omega$. This is called the *loading effect problem*; special techniques have to be employed to raise the effective resistance. This will be discussed in further details in section 3.3.

One of the first experiments involved placing a 1nH chip inductor (Coilcraft 0402CS) in parallel with a 100pF chip capacitor (ATC 650F). The dielectric of the circuit board was FR-4 with ϵ_r of 4.6. The dimensions of the coplanar waveguides were a=0.7mm, b=2.25mm, t=0.001mm, h=1.57mm, length=50mm. According to equations 3.1 to 3.3, ϵ_{eff}=2.42 and $Z_o = 97\Omega$. The separation between the center conductor and the ground planes (b-a) was mainly determined by the size of the shunt chip components. The measurement results are summarized in figures 3-6 to 3-10. The S_{21} data in fig. 3-6 shows a resonant peak at 221MHz and an inverted peak at 310MHz. The resonant frequency due to the LC combination of L=1nH and C=100pF is expected to be about 500MHz. The discrepancy was due to the parasitics of the circuits. To estimate a more accurate model of the actual circuit, we first extract the stray inductance L_S of the chip capacitor from the position of the inverted peak, which is calculated to be 2.6nH. The parasitics L_2, L_3 and L_4 are the stray inductances along the center trace of the co-planar waveguides and are calculated to be 8nH, 2.4nH and 10nH respectively based on the waveguide dimensions. Referring to fig. 3-9, resonance occurs when the impedance of C_1, L_S, L_1, and L_3 add up to zero, in which case current will circulate around the loop marked by the four nodes. With the estimated values of the parasitics, the resonant frequency corresponding to the above four elements is estimated to be 205MHz, which is much closer to the measured value.

Figure 3-10 shows the PSPICE calculation of the S_{21} response with the parasitics taken into account. It agrees well with the actual data within uncertainty and indicates the validity of the estimated parasitics.

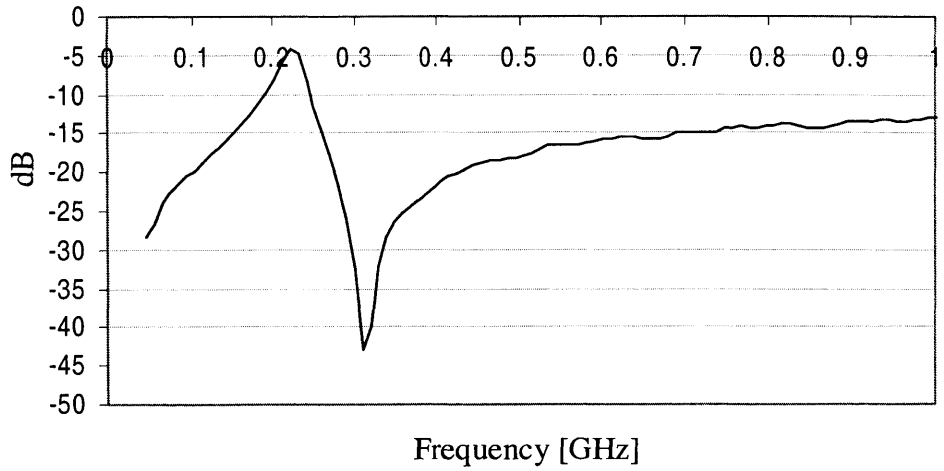

Figure 3-6: S_{21} measurement data. The resonant peak occurs at frequency f_o = 221MHz with a Q of 10.4. The inverted peak was due to the self resonance of the chip capacitor and occurs at f_{os} = 310MHz.

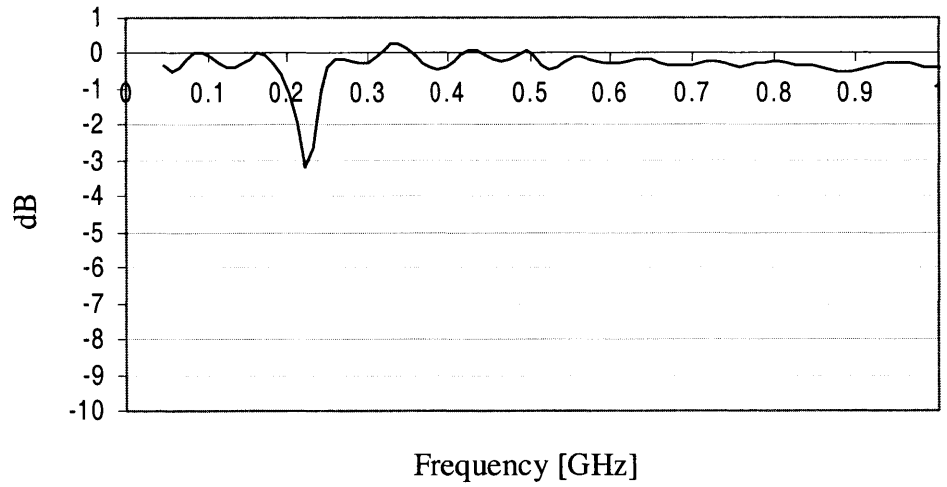

Figure 3-7: S_{11} has a minimum at the exact same frequency where a resonance was observed in the S_{21} measurement (221MHz). The signature due to the capacitor self-resonance was not evidenced.

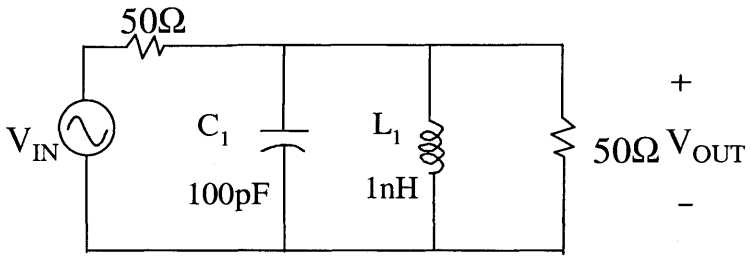

Figure 3-8: Circuit schematic of the network analyzer measurement. The source and output impedances are both 50Ω and matched to the 50Ω cables at both ends. The analyzer feeds in a voltage source V_{IN} and measures V_{OUT} across the 50Ω output impedance. The resonant circuit is a chip capacitor C_1 of 100pF in parallel with a chip inductor L_1 of 1nH. The parasitics of the circuit are ignored in this diagram.

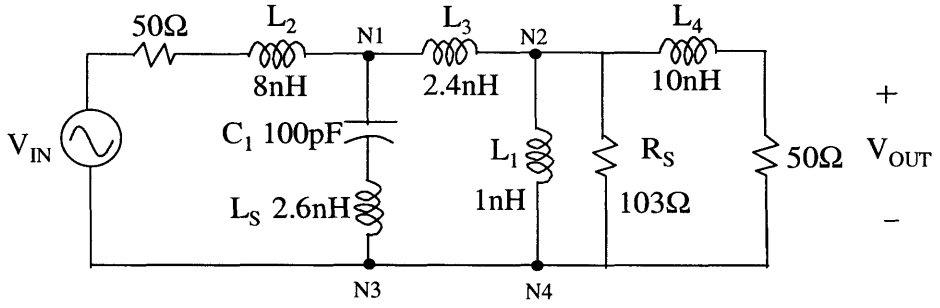

Figure 3-9: More accurate estimation of the actual circuit with parasitics considered. L_S and R_S are chip-component related. L_S is the stray inductance within the chip capacitor, and R_S is the stray resistance of the chip inductor. L_2, L_3 and L_4 are the stray inductances due to the center trace of the coplanar waveguides.

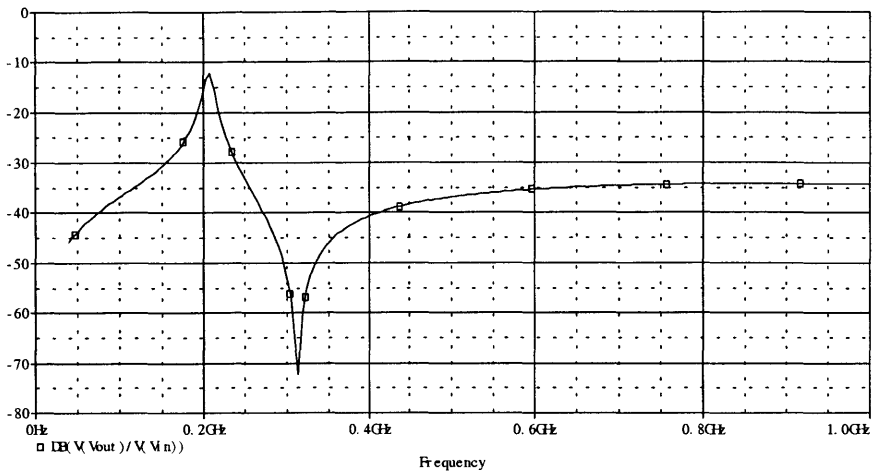

Figure 3-10: PSPICE simulation of the S_{21} response of the circuit in fig. 3-9. The resonant peak is calculated to be at 208MHz with a Q of 17. The inverted peak occurs at 312MHz. The simulation agrees well with the actual data within uncertainty.

The 100pF chip capacitor was then replaced by a 10pF capacitor, and the experiments were repeated using the same circuit board design. The results are summarized in figs. 3-11 to 3-14. The change of the capacitance from a high to a low value affects not only the resonant frequency, but also the sharpness of the peak. It can be seen from figure 3-11 that the resonant peak due to the 10pF capacitor suffers from a much lower Q. Recall that $Q = \frac{R_{eff}}{X_C}$, where $X_C = \frac{1}{\omega C}$, hence Q decreases with the value of the capacitance. This is the reason why when designing a resonant circuit, although the same resonant frequency can be achieved with several combinations of L and C values, the optimal Q is obtained when the inductor is a small value and the capacitor is a large value.

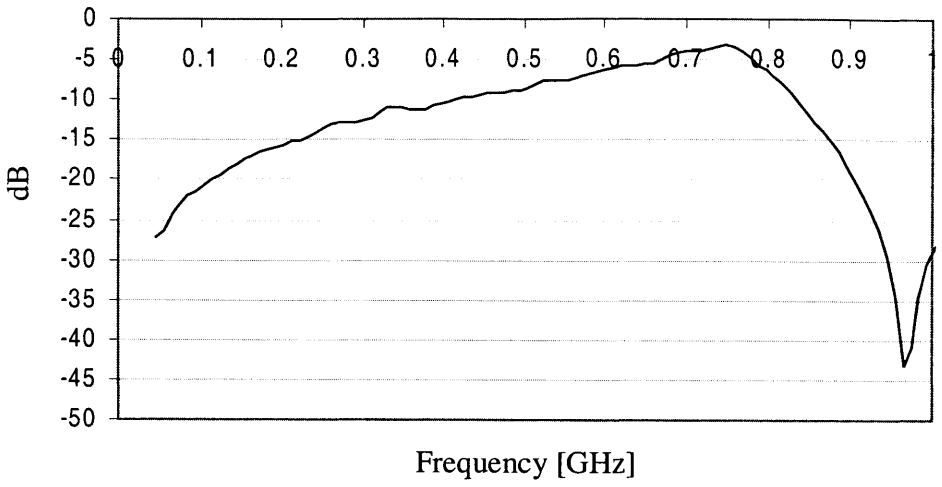

Figure 3-11: S_{21} measurement data with C replaced by 10pF. The resonant peak is identified at f_o = 749MHz yet suffers from a very low Q of 3.8. The inverted peak due to the self resonance of the chip capacitor occurs at f_{os} = 970MHz.

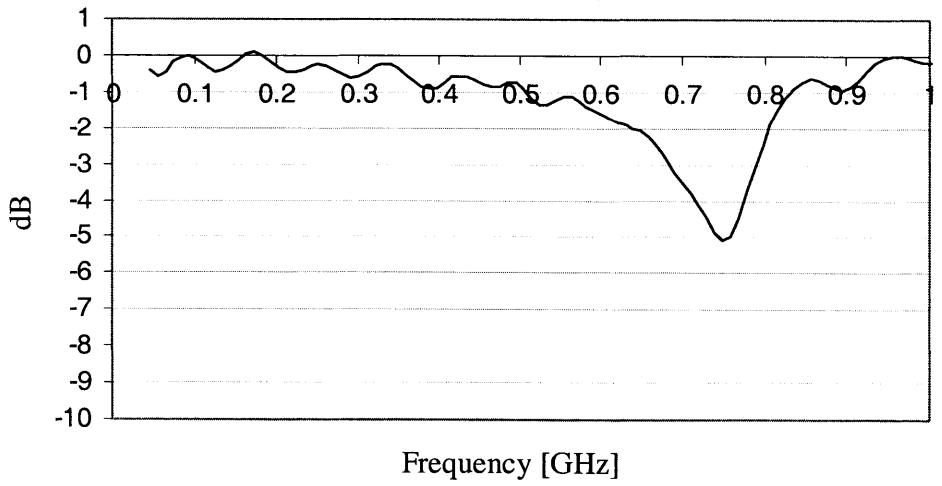

Figure 3-12: S_{11} has a minimum at 749MHz, where the resonant peak was also observed in the S_{21} measurement. This is consistent with the 100pF capacitor case.

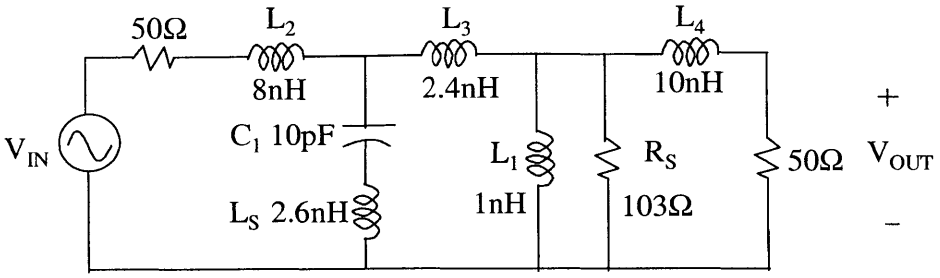

Figure 3-13: Actual circuit with parasitics included. The capacitor is 10pF and the associated stray inductance L_S is extracted to be 2.7nH from the position of the inverted peak. This is comparable with the stray inductance for the 100pF case (2.6nH) for the packaging of the chips is the same.

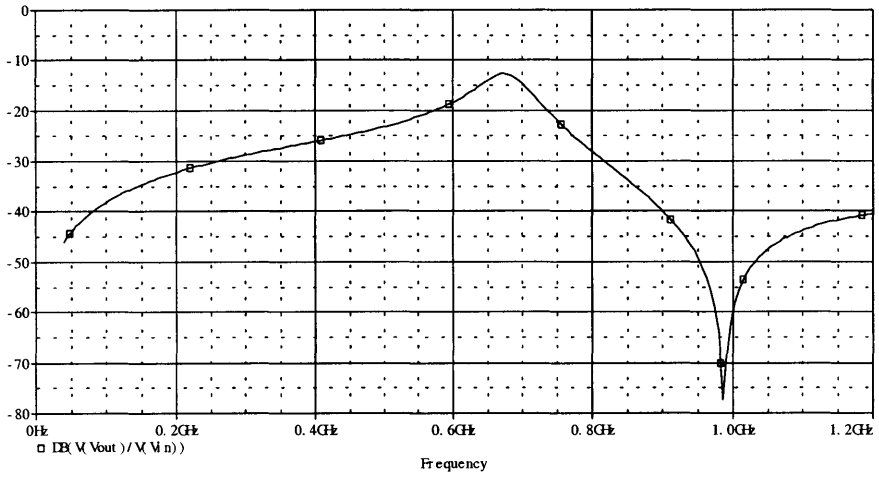

Figure 3-14: PSPICE simulation of the S_{21} response of the circuit in fig. 3-13. The resonant peak is calculated to be at 675MHz with an expected Q of 9. The inverted peak occurs at 985MHz.

3.3 Improved Resonant Circuit for Inductance Measurement

3.3.1 Background on Impedance Transformation and Impedance Matching

As we have seen earlier, the low values of the source and load impedance tend to load a given resonant circuit and decrease its Q. One way in overcoming this loading effect is to incorporate an impedance transformer to step the source/load impedance to a higher value. For the inductance measurement, we have chosen to use the so-called *tapped-L transformer*. It involves a split inductance where the ratio of the number of coils in each separated section corresponds to the factor by which the impedance is increased. Figure 3-15 illustrates a transformation of the load impedance and the equivalent resultant circuit "as seen" by the resonant circuit (fig. 3-16). R_L is transformed to $R_L^{'}$ according to the equation:

$$R_L^{'} = R_L(\frac{n_t}{n_1})^2 \tag{3.26}$$

where n is the number of coils, and is proportional to L. Thus, eqn. 3.26 can be rewritten as:

$$R_L^{'} = R_L(\frac{L_t}{L_1})^2 \tag{3.27}$$

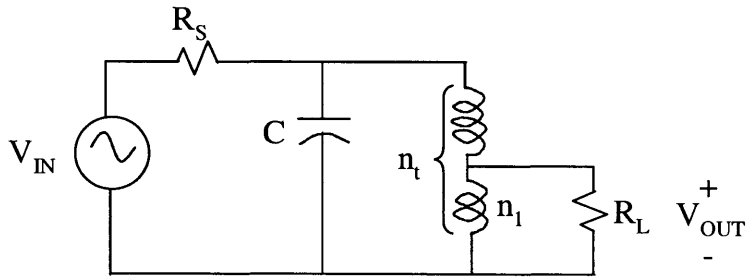

Figure 3-15: Tapped-L circuit in which R_L is transformed by the square of the ratio of the turns $n_t : n_1$

Note that there is a equivalent transformation which involves a split capacitance instead of inductance. Such an approach was not selected because it requires a capacitance of very high value and poses difficulty for on-chip fabrication.

Very often, impedance matching is also employed to RF circuits to maximize the power transfer between the source and the load. This is particularly important for

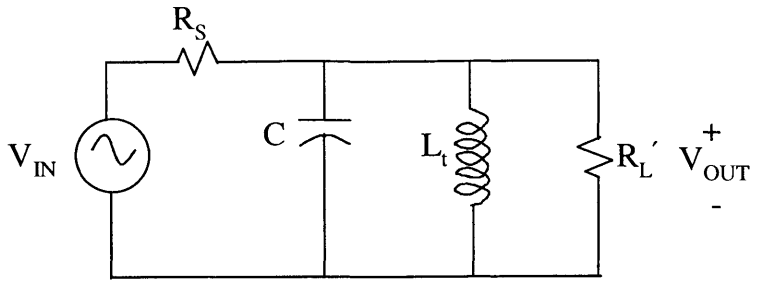

Figure 3-16: Equivalent circuit

the SQUID inductance measurement, since the input current (and hence power) that can be passed through the SQUID is limited by its critical current, and hence the output signal is extremely small.

Maximum power is transferred to the load when the load impedance is made to equal the *complex conjugate* of the source impedance. This can be achieved by a matching circuit called the L-network. It comprises an inductor and a capacitor which orient in the shape of a 'L'. Figure 3-17 shows a low-pass version of that (series inductor and shunt capacitor), and represents a particular case when the source and load are purely real. In general, they can be complex impedances.

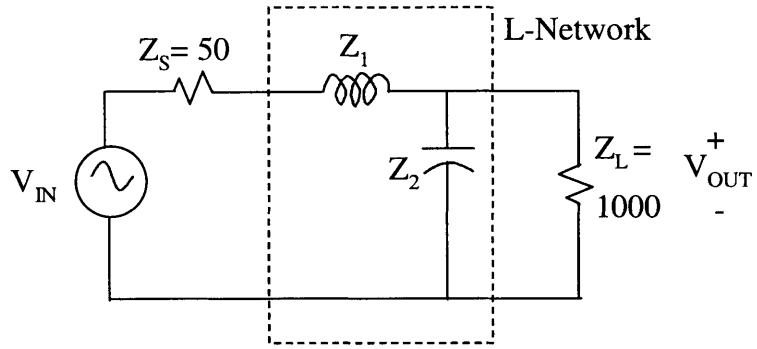

Figure 3-17: An example of a low-pass L-network used to match a 1000Ω load to a 50Ω source. In general Z_S and Z_L can be complex.

The way it works is that the shunt capacitor branch introduces some complex impedance $Z_2 = -j(\frac{1}{\omega C})$, where C is carefully chosen so that its shunt combination with the 1000Ω load will give a complex load of $50 - jX$ (fig. 3-18). Finally, the series inductor is chosen so that $Z_1 = j\omega L$ cancels with $-jX$, leaving only the 50Ω which matches with the 50Ω source. Note that the reactance of L and C are functions of frequency, and thus the matching can only be optimized at one single frequency. For cases when the impedances to be matched are complex, an additional reactive

component has to be inserted to "resonate" or cancel out the reactive impedance, and then the remaining real impedances can be matched as above.

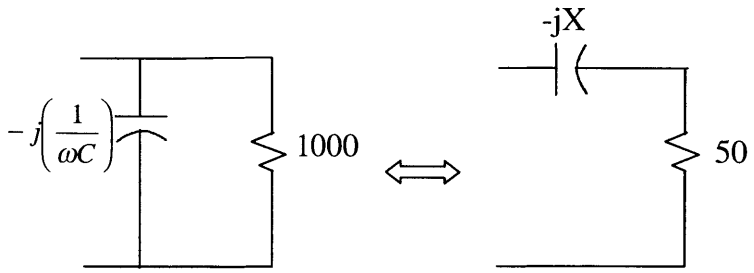

Figure 3-18: The capacitive branch turns the overall load into 50-jX, where -jX is later cancelled out by the series inductor.

3.3.2 Resonant Circuit for Inductance Measurement

With the knowledge we gathered from some simple parallel LC circuits which were tested at room temperatures, our next goal is to optimize a resonant circuit for the inductance measurement.

The first concern is that the SQUID inductance is even smaller than the 1nH chip inductance that we used. It is about 0.2nH to 0.7nH from the Lincoln parameters. To bias the resonant frequency at about 500 MHz, one would need a capacitor of about 500pF. Not only that such high a capacitance is not practical as far as on-chip fabrication constraints are concerned, it is also undesired for microwave measurements because high capacitance is associated with large parasitics. For our designs, we will keep the capacitor between 10pF to 100pF. Our solution is to add a bias inductor which resonates together with the capacitor and the SQUID, and consequently helps lower the overall resonant frequency. This bias inductor also has a double duty for the tapped-L transformer configuration.

The second concern is that the change in the SQUID Josephson inductance due to the qubit signal is also very small. In view of that, the resonant peak has to be as sharp as possible to maximize the voltage signal. The tapped-L transformation technique will be used to raise the Q of the circuit.

Finally, it is important to maximize the amplitude of the resonant peak as much as possible. As mentioned above, one is really limited on the input power that can be passed through the resonant circuit while still keeping the SQUID below its critical current. The L-network will be employed to ensure maximum power transfer.

A circuit was designed with the above techniques and is shown in fig. 3-19. Keep in mind that the goal at this stage is to have a prototype circuit built with chip components and readily tested at room temperature with a network analyzer. The values of the chip components are limited, and as will be seen later the final circuit parameters were slightly different from the optimal design. The inductance transformer is split into 5.6nH and 1.6nH, which steps the output resistance up by a factor of 20, i.e. from 50Ω to $1k\Omega$. The equivalent circuit is shown in fig. 3-20. The 10pF shunt capacitor resonates with a total equivalent inductance of 7.2nH to give a resonant frequency of about 600MHz. At resonant frequency, the capacitive impedance cancels out with the 7.2nH inductive impedance, we are left to match a real 1k load resistance to a source resistance of 50. Some calculations will show that this can be achieved with a L-network made up of a series inductor of 69nH and a shunt capacitor of 1.4pF. The 1.4pF capacitor can be combined with the 10pF to give a total of 11.4pF shunt. Due to the limited values available from chip components, circuit 3-21 was built instead, and its transfer characteristics were measured and shown in fig. 3-22. Comparing this with the previous results from the simple shunt of 10pF and 1nH (fig.3-11), the Q is significantly improved from 3.8 to 14.

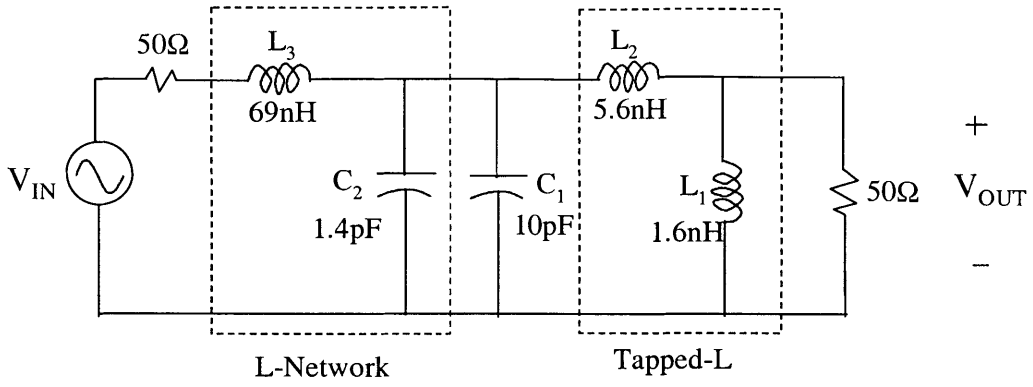

Figure 3-19: Resonant circuit improved with L-network matching and Tapped-L impedance transformation.

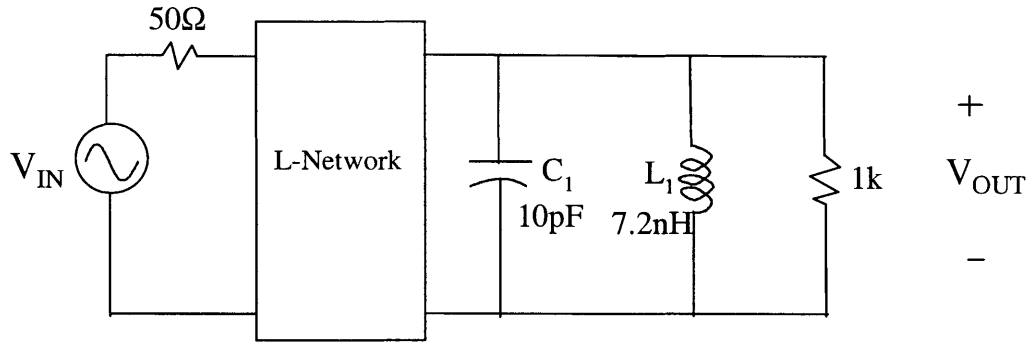

Figure 3-20: Equivalent circuit showing the transformed load.

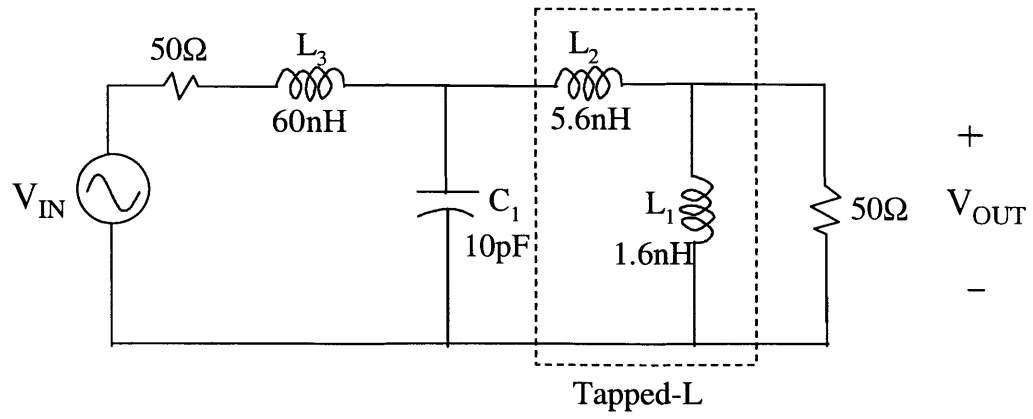

Figure 3-21: Actual circuit built with surface mount components.

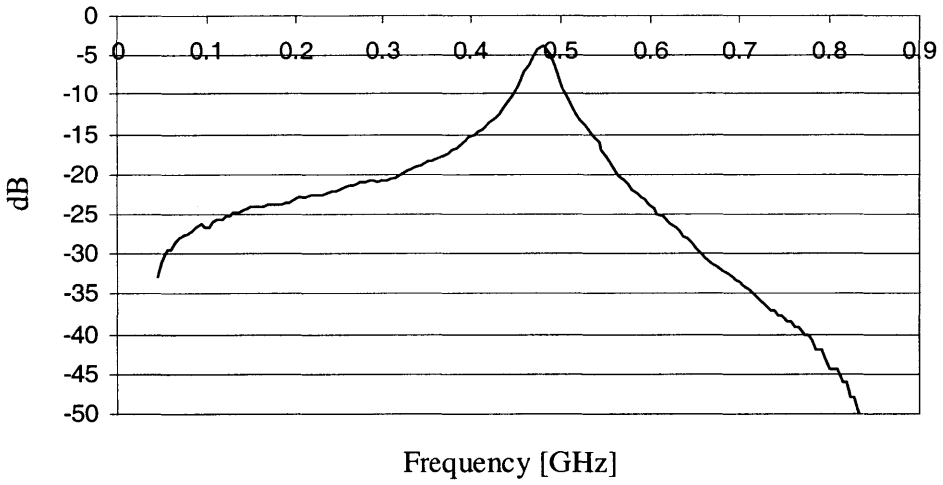

Figure 3-22: S_{21} measurement data. The resonant frequency is at 480MHz with an improved Q of 14. The discrepancy is due to the stray inductance of the co-planar waveguides and circuit components

3.4 RF Measurement Setup at 4 Kelvin

The experiments discussed so far were carried out at room temperature with the SQUID replaced by a chip inductor. Further experiments involving a SQUID have to be carried out at 4 kelvin, and later at dilution refrigerator temperatures. A helium-4 probe was set up with co-axial cables and the transmission characteristics were measured. In addition, the characteristics of the chip capacitors were also measured with the probe at 4K. Finally, the parasitics of the wire bonds will be discussed.

3.4.1 Characteristics of He-4 Co-axial cables

The helium-4 insertable cryostat manufactured by Janis Research Company was equipped with a pair of UT-85-B-B semi-rigid coaxial cables. The end of the cables near the sample end was attached with SSMC connectors. Owing to the limited space in the sample stage, SSMC connectors were chosen over the SMA or 3.5mm connectors for their micro-miniature size. The transmission properties of the cryostat was tested with a network analyzer, and the S_{21} characteristic is shown in figure 3-23. The cables exhibit increasing but acceptable loss with higher frequency. The loss is to be accounted for by calibrating the network analyzer in future measurements.

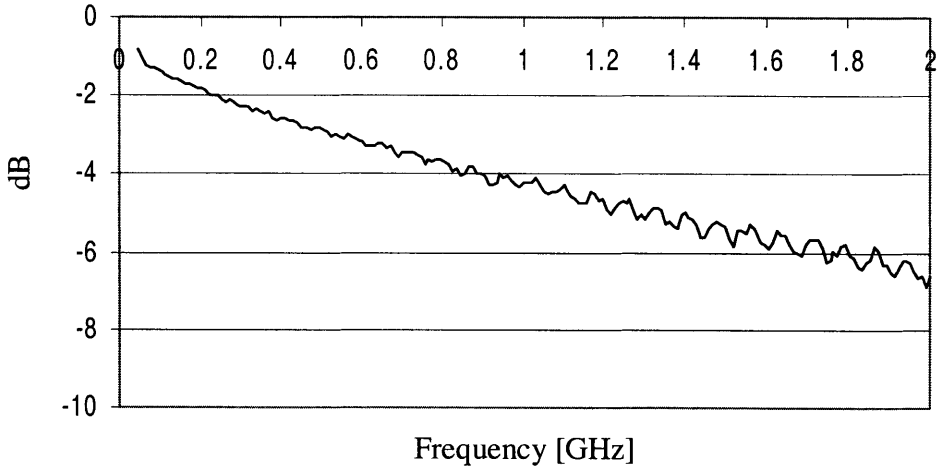

Figure 3-23: S_{21} characteristics of the UT-85 coaxial cables on the helium-4 cryostat. The maximum loss at 2GHz is -7dB.

3.4.2 Properties of chip capacitors at 4 Kelvin

The performance of the ATC 650F series chip capacitors at 4 kelvin was tested with the cryostat described above. Referring to figure 3-24, the performances at room temperature and at 4K are exactly the same. This confirmed that the capacitors can be used for off-chip low-temperature experiments.

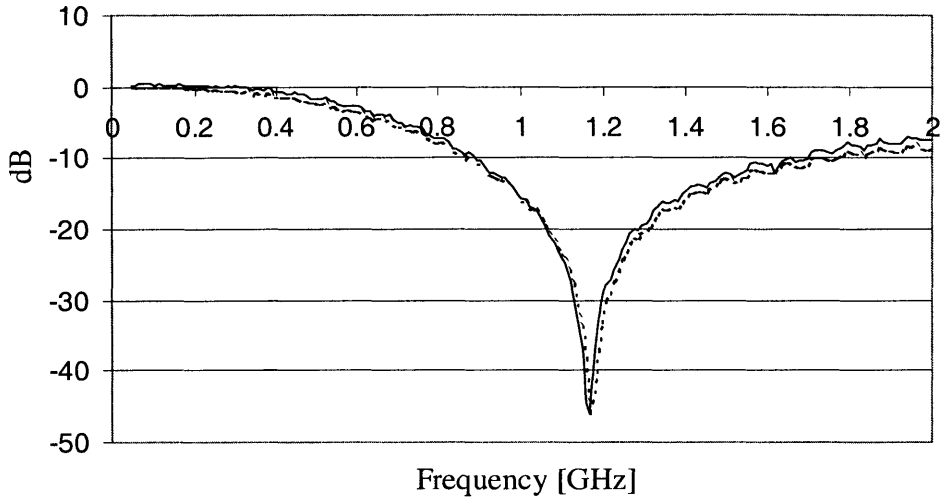

Figure 3-24: The S_{21} characteristics of a 10pF ATC 650F series chip capacitor. The solid line represents data at 4K and the dotted line at room temperature. The performances are the same within experimental uncertainty.

3.4.3 Parasitics of wire bonds

The results from the room-temperature experiments strongly suggest that the effect of the parasitics has to be taken into account. With the on-chip implementation of the circuits, some of the parasitics due to the bulk surface mount components can be avoided. A new source of parasitics will be introduced by the wire bonds. The diameter of the wire bonds is on the order of a thousand of an inch (mil), and the stray inductance of the wire is expected to be significant. The following experiment was carried out to measure the value of the stray inductance. As shown in figure 3-25, a single-layer capacitor (AVX SLC series) was wire-bonded from the center trace to the ground plane. The self-resonant frequency will be given by:

$$\omega_{os} = \frac{1}{\sqrt{[\frac{L_{bond}}{n} + L_{cap}]C}} \tag{3.28}$$

where L_{bond} is the stray inductance of one wire bond, and n is the number of wire bonds which vary from 1 to 3, and L_{cap} is the stray inductance of the capacitor packaging. Each gold wire bond is 1 mil thick and about 2.5mm long.

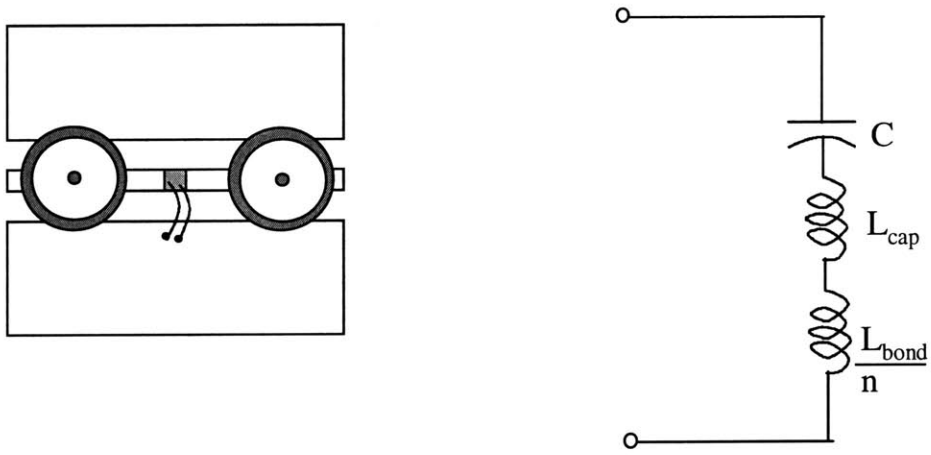

Figure 3-25: Illustration of how the capacitor is wire-bonded and the equivalent circuit model. L_{bond} is the stray inductance of one wire bond, and n is the no. of wire bonds which vary from 1 to 3. The overall bond inductance is given by $\frac{L_{bond}}{n}$ because the bonds behave like inductors in parallel.

The S_{21} transmission was measured and is shown in figure 3-26. We are mainly interested in the position of the self-resonant frequency f_{os} of the capacitor with the series stray inductances. To extract the stray inductance of a single bond, we can rearrange eqn. 3.28 as follows:

$$\frac{1}{\omega_{os}^2} = \frac{L_{bond}}{n}C + L_{cap}C \tag{3.29}$$

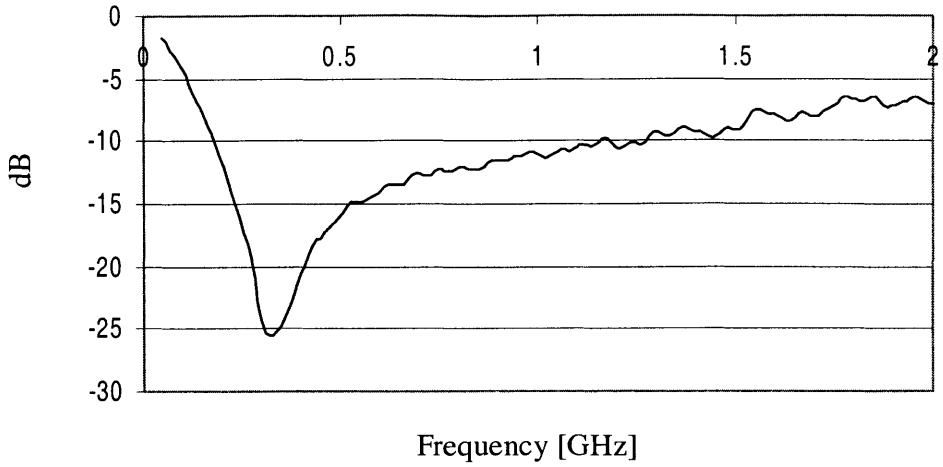

Figure 3-26: S_{21} measurement of the capacitor (100pF) in series with 2 gold wire bonds. The position of the dip is the self-resonant frequency.

Then a plot of $\frac{1}{\omega_{os}^2}$ vs. $\frac{1}{n}$ will have a slope that corresponds to $L_{bond} \times C$ and an intercept of $L_{cap} \times C$. The plot is shown in figure 3-27. For C=100pF, L_{bond} is extracted to be 1.4nH (per 2.5mm length), while L_{cap} is 1.6nH.

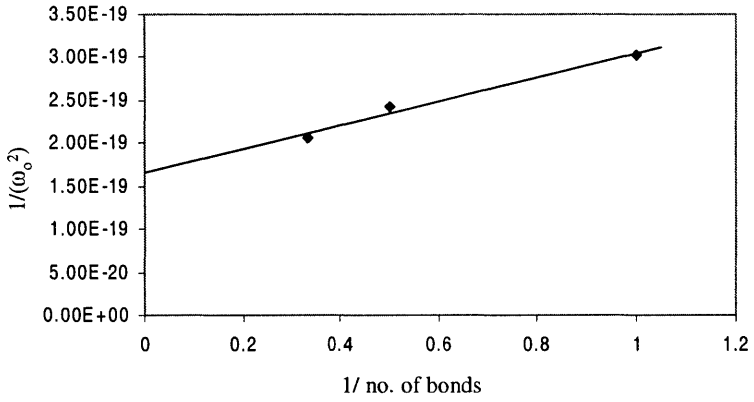

Figure 3-27: Plot of $\frac{1}{\omega_{os}^2}$ vs. $\frac{1}{n}$. For C=100pF, the parasitic inductance of one wire bond L_{bond} is extracted to be 1.4nH (per 2.5mm length), while the stray inductance due to the single layer capacitor L_{cap} is 1.6nH

Chapter 4

On-chip Circuit Designs with Calculations of Qubit Signal

Abstract

On-chip circuits were designed for the SQUID inductance measurement and will be in fabrication in Lincoln Laboratory under the run 'QC4'. The resonance properties of each of the circuits will be discussed, followed by a detailed analysis of their performance in the measurement process. In particular, the expected size of the signal due to the qubit flux will be calculated. Finally, the schematics of the RF electronics required for the inductance measurement will be briefly discussed.

4.1 On-chip circuit designs

In this section, we will present four on-chip circuits for the SQUID inductance measurement. All of the circuits are designed to resonate at about 500MHz, and have a high quality factor of at least 20. They are also optimized for power transfer with the peak voltage amplitude stronger than -10dB. These circuits also meet the fabrication constraints for the Lincoln fabrication process.

Conservative and aggressive SQUID junction parameters

Before introducing the circuit designs, it is important to get a sense of the SQUID parameters upon which the rest of the circuit parameters are determined. In general, the size of the Josephson inductance L_J for the typical SQUID parameters is extremely small. To optimize the qubit signal detected by the inductance measurement, the SQUID should have as large an L_J as possible. In this way, the absolute change in inductance due to a certain flux signal will be larger as well. Since L_J is inversely proportional to the critical current I_c, we have to push for the limit of fabricating Josephson junctions with the smallest I_c possible. This not only poses a challenge in fabrication constraints, but also implies more demanding handling procedures as

junctions of low I_c are very susceptible to electro-static discharge (ESD) problems.

For a certain fabrication process, the critical current density of the junction J_c is usually fixed. This value is between $100\,\mathrm{A/cm^2}$ to $200\,\mathrm{A/cm^2}$ for the Lincoln process (or $1\mu A/\mu m^2$ to $2\mu A/\mu m^2$). One is therefore left with a choice of the junction size to determine I_c. Two sets of SQUID junction parameters were used in the QC4 run and are summarized in the following table. The inductance values are based on the biasing conditions at $\Phi = 0.67\Phi_o$ and $I_L = 0.3I_C$. The 'conservative' SQUID has a bigger junction size and have been previously fabricated and measured at MIT with success. The 'aggressive' SQUID has even smaller junction size yet to be tested out. As will be seen later, the circuit parameters have to be slightly modified for each SQUID, but the overall design is essentially the same.

SQUID	Conservative			Aggressive		
Bias Points	$\Phi = 0.67\Phi_o$, $I_L = 0.3I_c$					
μm^2	1.1×1.1			0.6×0.6		
$J_{co}[\mu A/\mu m^2]$	1	1.5	2	1	1.5	2
I_C $[\mu A]$	2.42	3.63	4.84	0.72	1.08	1.44
L_J [nH]	0.34	0.23	0.17	1.13	0.76	0.57

4.1.1 Design 1: Tapped-L circuit with 10pF resonance capacitor

Figure 4-1 shows the circuit diagram of the first design for a conservative SQUID. The SQUID has a L_J of 0.225 nH and is shunted by a total capacitance C_{shunt} of 10 pF across the junctions. The advantages of this shunting capacitor have been confirmed both in the experiments at MIT and Delft. The large capacitance corresponds to a more massive particle in the shunted-junction model and serves to suppress fluctuations and narrow the distribution of the measured switching currents. In addition, it relieves the electro-static discharge (ESD) problems with the junctions by providing an alternative path for the high frequency noise to by-pass the junctions. However, the side-effect of the shunting capacitance is that it resonates with L_J to give an additional resonant peak, which has to be kept out of the qubit frequency range as well as the 500MHz inductance measurement range. The value of 10pF was chosen based on the decoherence calculations which will be presented in chapter 5. It corresponds to a peak at about 3.5 GHz, slightly below the qubit frequencies.

The transfer function is shown in fig. 4-2. The resonant peak for the inductance measurement has a position of 596MHz and a Q of 23. This occurs when the 10pF capacitor C_{res} resonates with the sum of L_J, L_1, and L_2 which total 7nH. The 'resonating loop' is denoted by nodes N1 to N4 in fig. 4-1. Note that this 10pF resonance capacitor is not to be confused with the shunting capacitance across the SQUID, which also happens to be 10pF.

The voltage output is tapped across a split inductance configuration. We know from section 3.3 that this so-called tapped-L configuration transforms the 50Ω output resistance to a higher resistance depending on the square of the ratio of the split inductances. For the values used here, the 50Ω is stepped up by a factor of 20 to $1k\Omega$. The L-network matches the resultant $1k\Omega$ output resistance to the 50Ω source. It comprises the 69nH inductor and a 1.4pF capacitor. At the resonant frequency, the impedances of the loop N1-N4 add up to zero and thus can be ignored as far as impedance matching is concerned.

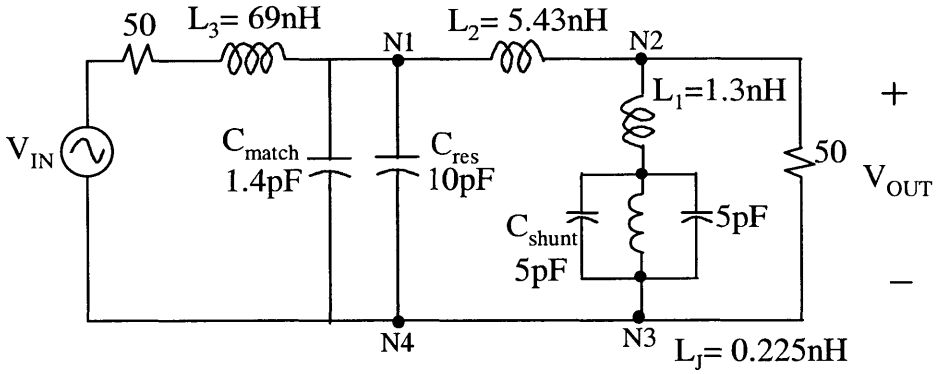

Figure 4-1: Circuit 1: Tapped-L circuit with 10pF resonance capacitor for the 'conservative' SQUID

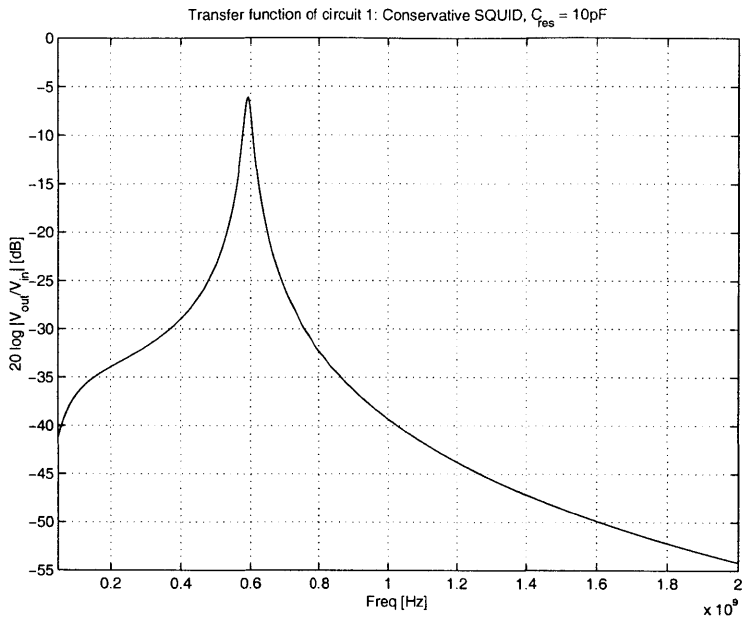

Figure 4-2: Transfer function of circuit 4-1. The peak is at 596MHz with amplitude -6.3dB and a Q of 23.

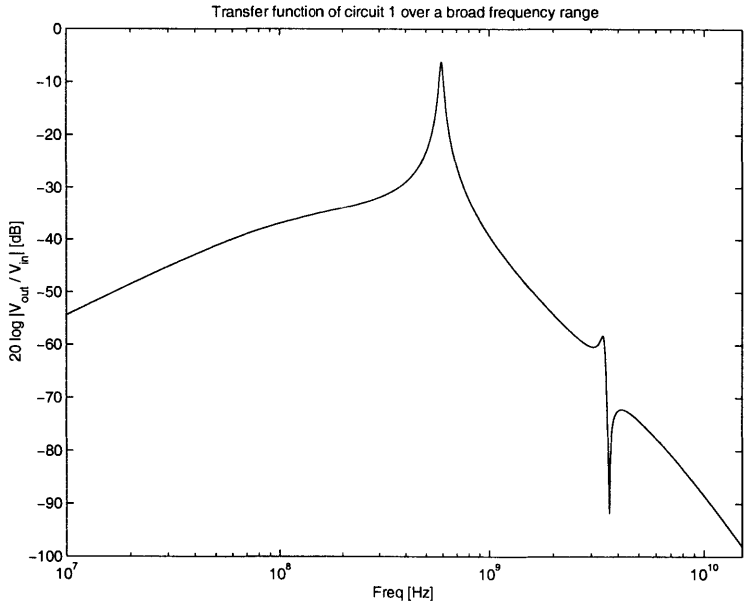

Figure 4-3: Transfer function of circuit 4-1 plotted over a wider frequency range in a log scale. The second peak at 3.5GHz is due to the shunting capacitor across the SQUID

Figure 4-4 is a similar design modified for the SQUID with aggressive parameters. L_J is now 0.756 nH. The only adjustment is that L_1 is now 0.8nH instead of 1.3nH as for the conservative SQUID. Its transfer function is shown in fig.4-5. The peak is at 587MHz with a Q of 23.

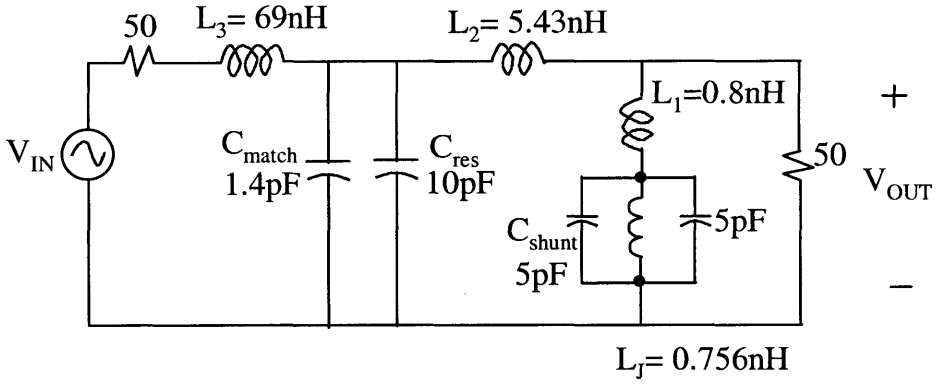

Figure 4-4: Circuit 2: Tapped-L circuit with 10pF resonance capacitor for the 'aggressive' SQUID

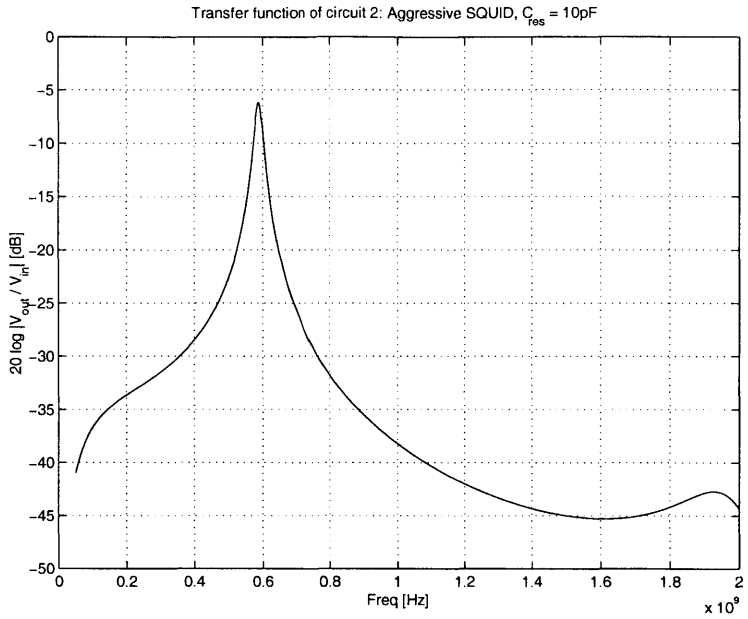

Figure 4-5: Transfer function of circuit 4-4. The peak is at 587MHz with amplitude -6.3dB and a Q of 23. The second peak at about 1.9GHz is due to the shunting capacitor across the SQUID.

The role and drawback of the biasing inductors

The design for both circuits 1 and 2 has used two biasing inductors L_1 and L_2 which are worth discussing here. Owing to the small value of L_J, they are introduced to lower the resonant frequency to about 600MHz which will otherwise be in the GHz regime. However, the absolute change of the inductance due to the qubit signal will be smaller due to the presence of these constant bias, and the sensitivity of the measurement will decrease. In the next design, this problem will be improved at the cost of raising the resonance capacitor from 10pF to 100pF. Nevertheless, some biasing inductance is still needed to realize the tapped-L impedance transformation. One may propose to totally get rid of the biasing inductance and use a tapped-C configuration instead. However as mentioned before in section 3.3.1, this would involve using a capacitor as big as 1nF. This demands a huge chip space and cannot be realized with the Lincoln process.

4.1.2 Design 2: Tapped-L circuit with 100pF resonance capacitor

We now introduce the second design for the inductance measurement which uses a 100pF resonance capacitor, about ten times bigger than the capacitance of the previous design. The circuit diagram is shown in fig.4-6. The advantages of having a large

capacitance are that (1) it requires only a smaller inductance bias and thus improves the signal sensitivity, and (2) the quality factor Q of the circuit is raised since it is proportional to $\frac{R_{eff}}{X_c} \sim C$. However one should also be aware of its drawbacks: (1) the design occupies a larger chip space, (2) 100pF is much bigger than the capacitance typically fabricated in the Lincoln process and its performance is yet to be tested, and (3) for microwave measurements, a larger capacitance is usually associated with larger parasitics.

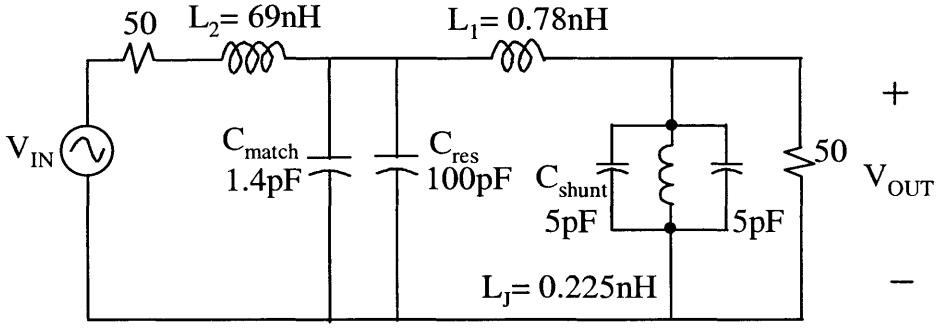

Figure 4-6: Tapped-L circuit with 100pF resonance capacitor for the 'conservative' SQUID

The transfer function is shown in figure 4-7. The resonant peak has a position of 500MHz and a Q of 150. The Q is significantly higher because a larger resonance capacitor is used. Only one biasing inductor L_1 is employed, and it also serves as the tapped-L transformer. Again, the 50Ω is stepped up to $1k\Omega$. The L-network impedance matching is the same as the previous design.

The circuit modified for the aggressive SQUID is shown in fig.4-8. From the transfer function in fig.4-9, the resonant frequency is at 495MHz with a Q of 46. Note that the 100pF resonance capacitor is replaced by a 30pF capacitor to get the right frequency bias.

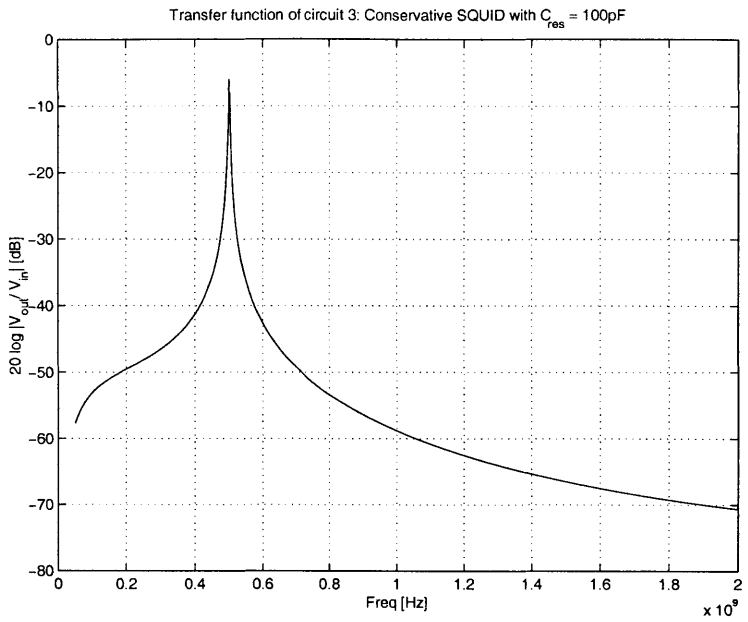

Figure 4-7: Transfer function of circuit 4-6. The peak is at 500MHz with amplitude -6.0dB and a Q as high as 150.

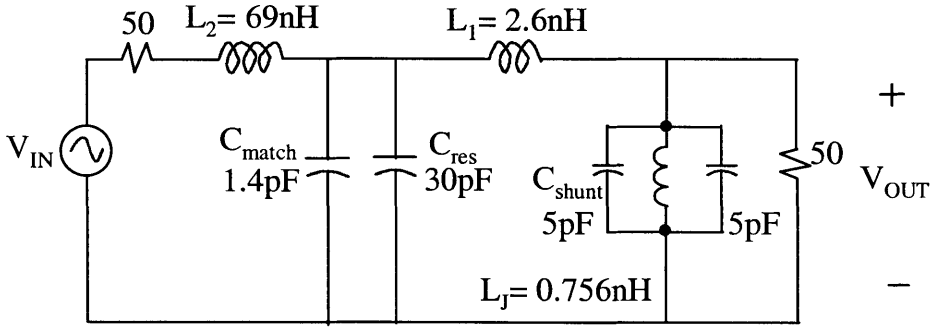

Figure 4-8: Tapped-L circuit with 30pF resonance capacitor for the 'aggressive' SQUID

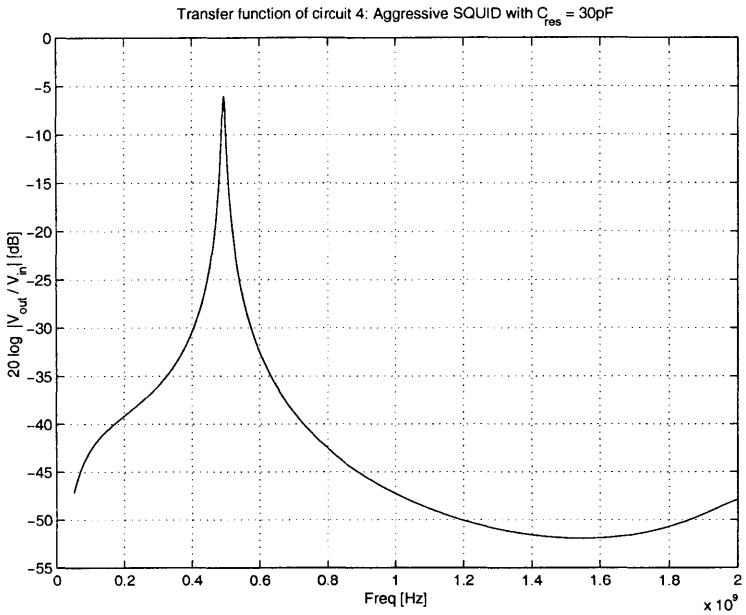

Figure 4-9: Transfer function of circuit 4-8. The peak is at 495MHz with amplitude -6.0dB and a Q of 46.

4.1.3 Qubit and SQUID coupling

For the inductance measurement, the qubit is coupled to the SQUID in the same way as the switching current method. It is placed inside the SQUID loop as in figure 4-10. The geometry and proximity of the loops determine the strength of the coupling M. In addition, since both the qubit and the SQUID are subject to the same *external* magnetic field, their area ratio sets the flux bias for the SQUID as the qubit is always biased very near $0.5\Phi_o$. To illustrate this more clearly, consider the case of biasing the SQUID at $0.67\Phi_o$, we can calculate the required area ratio as follows:

$$\begin{aligned} \frac{A_{SQ}|B|}{A_{Qubit}|B|} &= \frac{0.5\Phi_o}{0.67\Phi_o} \\ \frac{A_{SQ}}{A_{Qubit}} &= 1.3 \end{aligned}$$

For the above circuit designs, the inner dimensions of the qubit loop are $18\times18\mu m^2$ and that of the SQUID are $20.8 \times 20.8\mu m^2$. The width of the SQUID trace is $1\mu m$ and the qubit trace is $0.7\mu m$. A simulation with the software Fast Henry calculates the mutual inductance to be M=30.5pH. The loop inductance is 53pH and 64pH for the qubit and SQUID respectively. For comparison, the value of M used at Delft is 8pH. Due to the stronger coupling, we expect a larger qubit signal of $0.01\Phi_o$, about

10 times larger than the signal at Delft which is $0.0015\Phi_o$. On the other hand, decoherence calculations in chapter 5 will show that the relaxation time in our system is about 50 times shorter. The dimension of the bigger and smaller qubit junctions are $1 \times 1\mu m^2$ and $0.9 \times 0.9\mu m^2$ respectively. The constant α is 0.65.

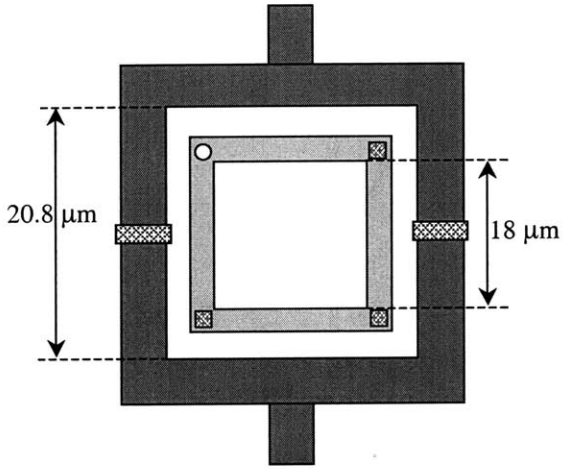

Figure 4-10: The layout of the qubit inside a SQUID loop. The patterned boxes represent the junctions, and the circle represents a via hole.

4.1.4 Spiral Inductors

Inductances of the on-chip designs were implemented by a planar spiral configuration. Square spirals were chosen for the ease of the layout. There exists numerous mathematical models to estimate the inductance of a certain layout. In our case, the expected values are simulated using the software Fast Henry. The L-shaped matching network in the designs involves a relatively large inductance of 69nH. The performance of the spiral layout therefore needs to be optimized as much as possible. Some useful strategies for designing spiral inductors will be presented in appendix B.

4.2 Calculation of Voltage Signal

So far, we have been focusing on the resonant characteristics of the circuit designs. We will now take a step further and analyze the performance of the circuits in the inductance measurement process. The basic ideas of the measurement scheme has been outlined in section 2.2 and will be described in details here. The actual parameters of the on-chip designs can now be used to address issues such as (1) the actual size of the shift in peak position upon the qubit flux, (2) the optimal DC and AC bias, (3) the side effects of the AC bias on the shape of the resonant peak, (4) the need for retrieving the flux information as a voltage signal and the way that can be achieved, and (5) the size of the optimal voltage signal.

As also discussed in section 2.2, the variation of the SQUID inductance in time with the oscillating current requires one to solve the non-linear differential equation in order to completely describe the dynamics of the resonant circuit. Based on the simulated results in [8] for a simplified resonant circuit, it is reasonable to believe that analyzing the inductance measurement scheme based on a semi-static approach assuming the SQUID as a lumped inductor (L_J given by eqn. 2-18) should give similar results. We will adopt this approach because it is particularly useful to help us get an intuitive understanding of the measurement method.

4.2.1 Inductance measurement with circuit 1: Conservative SQUID with 10pF resonance capacitor

Our first task is to find the right operating conditions for the SQUID. Recall that the Josephson inductance depends on two factors: the current through the SQUID and the magnetic flux that threads the loop. Thus, both the flux bias and the current bias have to be determined. Fig. 4-11 shows the dependence of L_J on flux between 0.6 to 1 Φ_o. This is the range of possible flux bias for the SQUID considering the qubit flux is biased very near $0.5\Phi_o$, and that the SQUID needs to have a bigger area than the qubit. It can be seen that L_J has a higher sensitivity to flux between 0.6 and 0.7 Φ_o than the operating point of $0.76\Phi_o$ that has previously been used in the switching current measurement. One should however be cautious not to get too close to 0.6 where L_J diverges. The bias is thus set to $0.67\Phi_o$. (the choice is partially influenced by the design rules for the qubit and SQUID layout) For the current bias, it is chosen to be $0.3I_c$ as that falls on the linear region of the plot and can avoid unwanted non-linear effects (fig.4-12). At the bias point with $\Phi = 0.67\Phi_o$ and $I_L = 0.3I_c$, the inductance L_J of the conservative SQUID with I_c being $3.63\mu A$ is 0.225nH (conservative SQUID parameters used before).

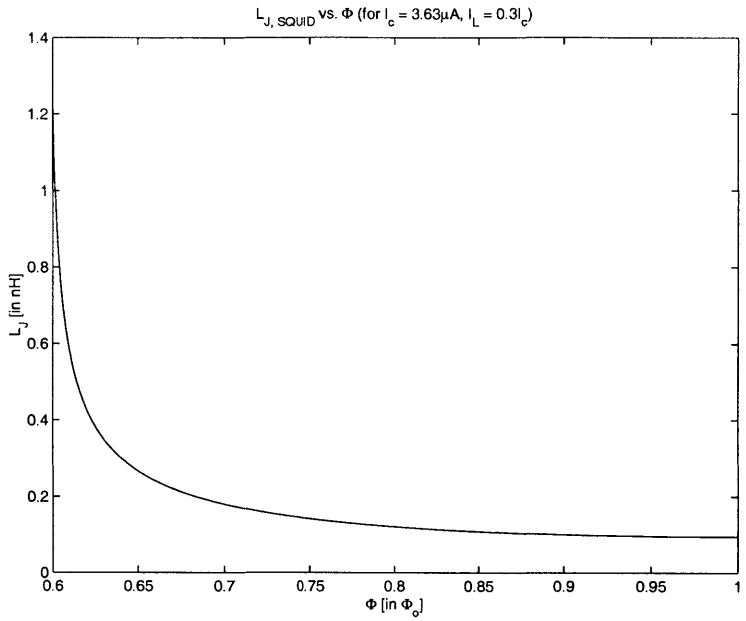

Figure 4-11: SQUID inductance as a function of external flux bias

To determine the optimal AC operating conditions, we must first consider the effect of the AC bias on the SQUID. As the current through the SQUID varies over an AC cycle, its Josephson inductance also varies accordingly. We will analyze this with a semi-static approach and calculate the inductance using the equation:

$$L_J = \frac{\Phi_o}{2\pi I_c |\cos(\pi\frac{\Phi}{\Phi_o})| \sqrt{1 - \frac{(I_{dc}+I_{ac})^2}{I_c^2 cos^2(\pi\frac{\Phi}{\Phi_o})}}} \tag{4.1}$$

L_J over a current cycle is plotted in figure 4-13. For illustrative purpose, we assume $I_{L,ac} = 0.1I_c\cos(\omega t)$, $I_{L,dc} = 0.3I_c$, and $\Phi = 0.67\Phi_o$.

As expected, the resonant peak position oscillates with L_J over a cycle as well. This is illustrated in figure 4-14. The actual shift of the complete transfer functions is shown in figure 4-15.

Since the actual qubit flux also manifests itself as a shift in resonant position, the AC oscillation in figure 4-15 has to be distinguished from the qubit signature. This can be achieved because the shift due to the AC variation varies over a cycle, while the shift due to the flux is independent of time. The AC effect will be approximated by taking the time average of the peak positions over a cycle to give a resultant peak which has a broader FWHM. The time-averaged peak is shown as dotted-line in fig.4-15. The flux signature will be an additional shift in the position of this dotted peak.

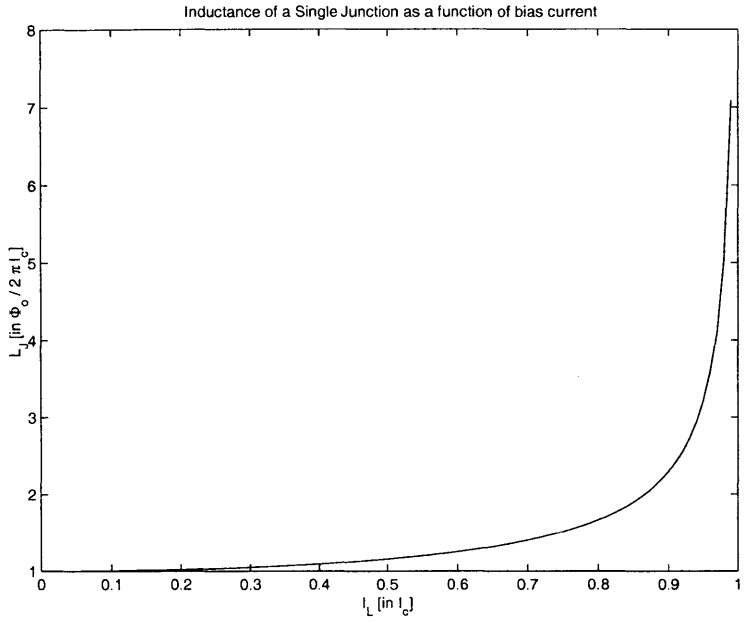

Figure 4-12: SQUID inductance as a function of bias current, with $\Phi = 0$

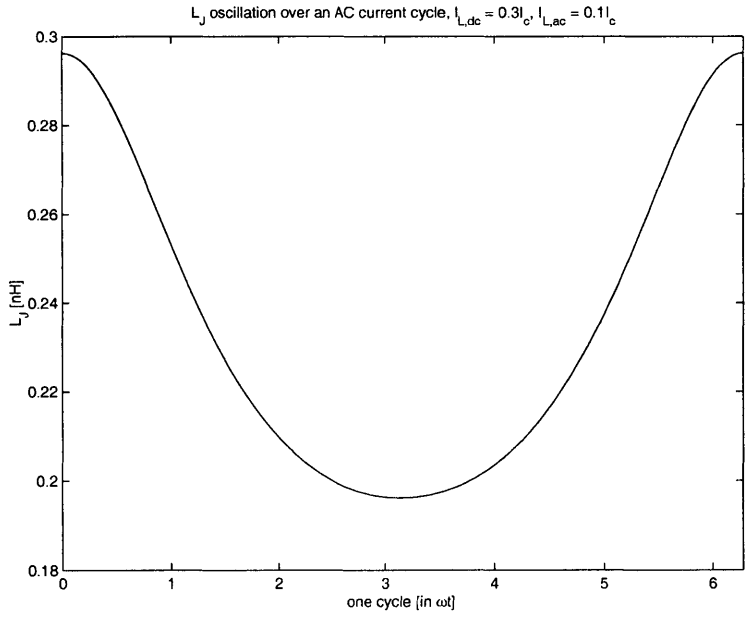

Figure 4-13: L_J oscillation over an AC current cycle.

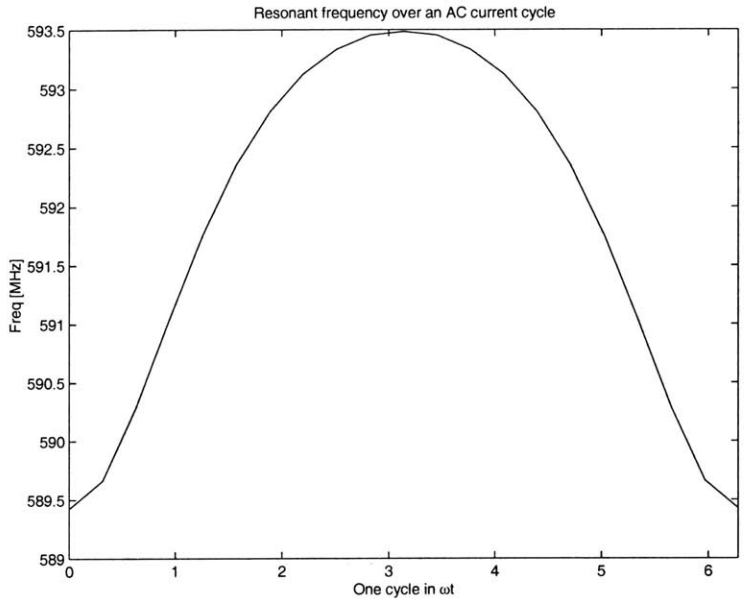

Figure 4-14: Oscillation of resonant frequency over an AC cycle.

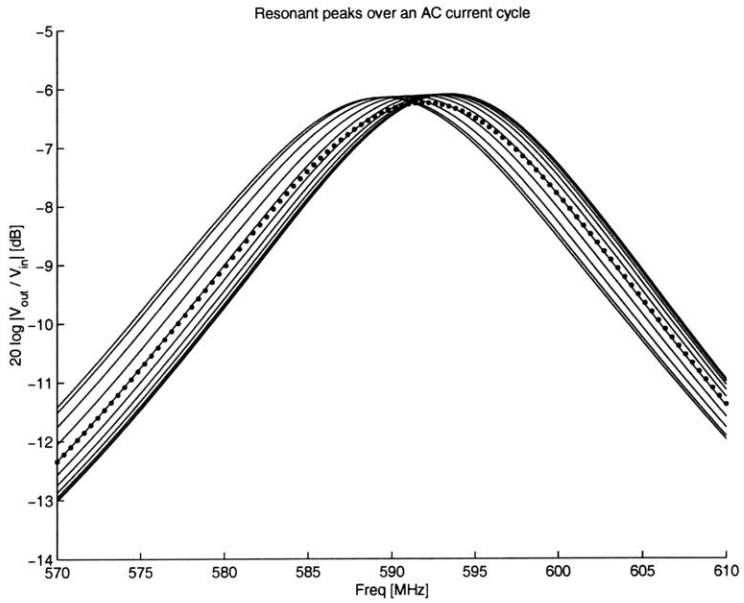

Figure 4-15: Illustration of how the resonant peak oscillates. The time-average is a broadened peak represented by the dotted line.

For the parameters at MIT, the junction sizes of the qubit and the strength of its coupling to the SQUID corresponds to a flux signal of about $0.01\Phi_o$, while the signal at Delft is $0.0015\Phi_o$. We have calculated the frequency shift for the MIT case and compared that with the Delft scenario. The results are summarized in the following table.

Circuit 1			
	Bias	MIT	Delft
Signal size $[\Phi_o]$	–	0.01	0.001
Flux Level $[\Phi_o]$	0.67	0.68	0.671
f_o [MHz]	592.3	593.0	592.5
Δf_o [MHz]	–	0.7	0.2

On the preliminary level, one may suggest observing the shift in peak position by measuring the transfer function with a network analyzer at the two flux values. To sweep a transfer function, the network analyzer sends down a constant voltage level from one port and measures the output signal at the other port over a range of frequency. However, at different frequencies, the impedance of each circuit element is not the same. This poses a problem of biasing the SQUID at the right current level. In particular, at low frequencies, more current will pass through the SQUID inductor, while at high frequencies, the current will be diverted to some other branches instead. It is therefore impossible to actually current bias the SQUID at the operating point over the whole frequency range. This means the measurement needs to be performed at one single frequency only.

The way this can be achieved is as follows. Consider the scenario of sending a single-frequency voltage source down the circuit. The output will also be at the same frequency with an amplitude depending on the voltage transfer ratio $\frac{V_{out}}{V_{in}}$ in dB (dB $= 20\log|\frac{V_{out}}{V_{in}}|$). Initially, at the flux bias of $0.67\Phi_o$, the output voltage is $V_{in} \times \frac{V_{out}}{V_{in}}|_i$. Upon the addition of the qubit flux, the resonant peak shifts to the right, and the transfer ratio as seen at the frequency bias will be reduced to dB_f, and the new output voltage is now $V_{in} \times \frac{V_{out}}{V_{in}}|_f$. Therefore the flux signal is now mapped to a difference in output voltage given by:

$$signal = \Delta V_{out} = V_{in} \times (\frac{V_{out}}{V_{in}}|_i - \frac{V_{out}}{V_{in}}|_f) \tag{4.2}$$

Note that $\frac{V_{out}}{V_{in}}|_i$ (or dB_i) is higher than $\frac{V_{out}}{V_{in}}|_f$ (or dB_f) because the peak shifts to the right. In addition, it is clear that the single frequency should be chosen as close to the resonant peak as possible because that region has the sharpest slope and is the most sensitive. For this particular circuit, the resonant frequency is about 590MHz, and so the frequency bias is chosen to be 580MHz. We are now in the position to consider what is the optimal voltage signal possibly achieved. Typically for a linear circuit,

V_{out} is a fraction of V_{in} according to the voltage divider. This may suggest that a larger V_{in} always gives a larger V_{out}. However, this does not apply to our circuit here because a SQUID is involved. Firstly, there is an upper limit to how much current that can be passed down a SQUID since it has to be biased along the supercurrent branch. Secondly, the Josephson inductance L_J of the SQUID actually varies with the size of I_L. A larger V_{in} leads to a larger AC current amplitude and the time-averaged peak will be broader due to the wider oscillation. In other words, as V_{in} increases, the resonant peak broadens, $dB_i - dB_f$ decreases and finally becomes negative when V_{in} reaches beyond a certain level. This is clearly illustrated in figures 4-16 to 4-17.

With all these factors taken into consideration, the size of the voltage signal as a function of input voltage is calculated and shown in fig.4-18. The optimal voltage signal is $2.4\mu V$.

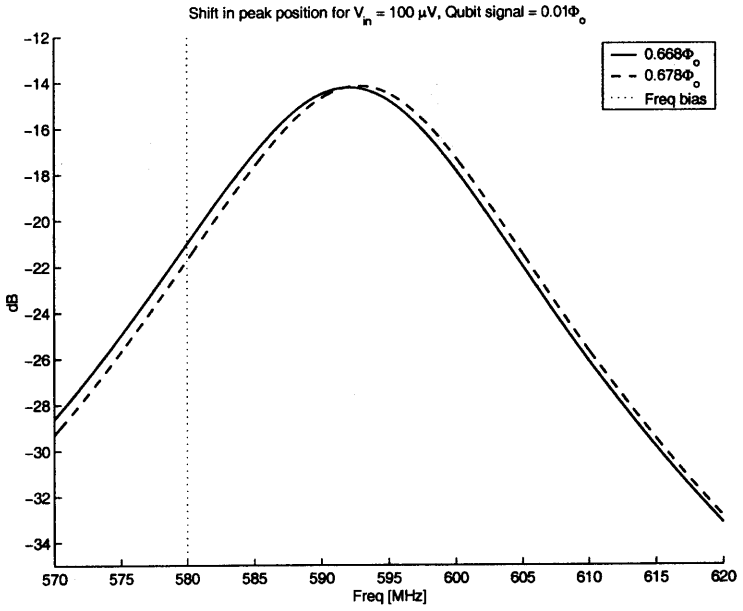

Figure 4-16: Case when $V_{in} = 10\mu V$. The solid line shows the peak at $\Phi = 0.67\Phi_o$; the broadening is due to an AC current amplitude of $0.079I_c$. The dotted line corresponds to the shifted peak at $\Phi = 0.68\Phi_o$; the broadening is caused by a current amplitude of $0.085I_c$. Note that the current amplitude is slightly different at the two flux levels even tough V_{in} is the same, because the different inductances also affect how much current actually passes through the SQUID branch.

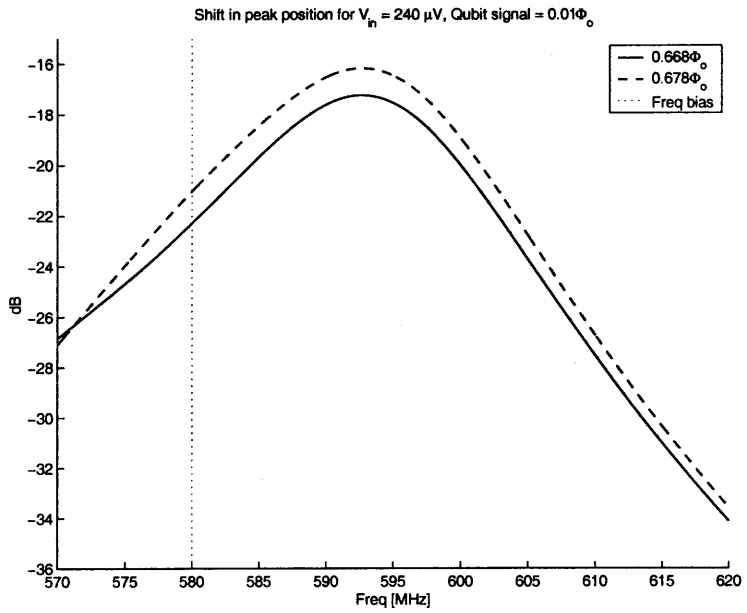

Figure 4-17: Case when $V_{in} = 240\mu V$. The peaks have been seriously broadened due to the large driving source. The difference in transfer ratio $dB_i - dB_f$ actually becomes negative.

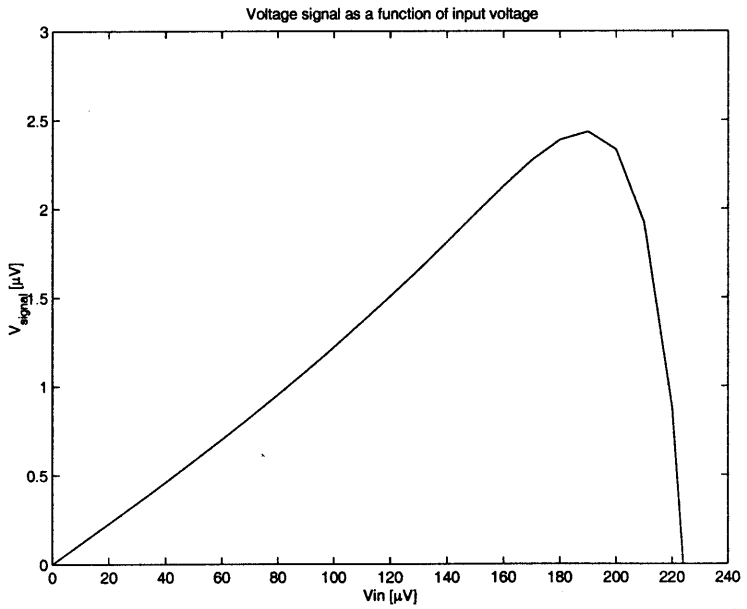

Figure 4-18: Voltage signal as a function of input voltage for circuit 1. The input voltage is only plotted for 0 to $240\mu V$ because above that the SQUID is no longer along the supercurrent branch. The optimal input voltage is $190\mu V$ yielding a voltage signal of $2.4\mu V$. This corresponds to a AC current amplitude of $0.15I_c$ through the SQUID. Beyond this point, the signal decreases and finally turns negative.

4.2.2 Inductance measurement with circuit 2: Aggressive SQUID with 10pF resonance capacitor

Similar analysis was performed for the remaining three on-chip circuit designs. Firstly, for the second design (fig.4-4), the Josephson inductance of the SQUID and the corresponding peak position at the two flux values are summarized in the following table:

Circuit 2			
	Bias	MIT	Delft
Signal size [Φ_o]	–	0.01	0.001
Flux Level [Φ_o]	0.67	0.68	0.671
f_o [MHz]	587.8	590.4	588.2
Δf_o [MHz]	–	2.6	0.4

The voltage signal as a function of input voltage is shown in figure 4-19. The optimal signal is $5.7\mu V$ corresponding to an input voltage of $175\mu V$ (amplitude of AC current through the SQUID is $0.1I_c$). The signal is twice that of the case for the conservative SQUID.

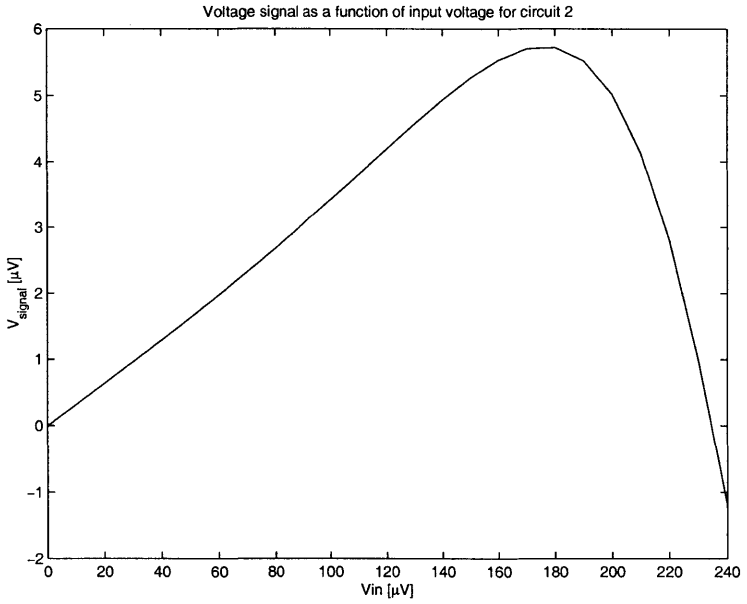

Figure 4-19: Voltage signal as a function of input voltage for circuit 2. The frequency bias is 570MHz. The optimal voltage signal is $5.7\mu V$ corresponding to an input voltage of $175\mu V$. This signal is about twice that of the conservative SQUID.

4.2.3 Inductance measurement with circuit 3: Conservative SQUID with 100pF resonance capacitor

The table summarizes the results for the third design (fig.4-6). It should be pointed out that the shift in peak position is significantly larger than the previous two designs due to the smaller biasing inductance.

Circuit 3			
	Bias	MIT	Delft
Signal size [Φ_o]	–	0.01	0.001
Flux Level [Φ_o]	0.67	0.68	0.671
f_o [MHz]	500.8	501.8	505.4
Δf_o [MHz]	–	1	3.6

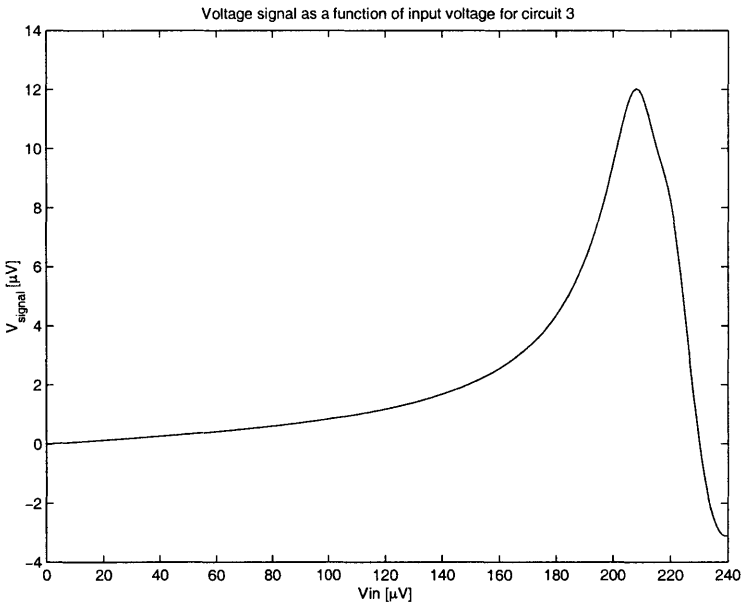

Figure 4-20: Voltage signal as a function of input voltage for circuit 3. The frequency bias is 475MHz. The optimal voltage signal is $11.8\mu V$ corresponding to an input voltage of $210\mu V$. Although a conservative SQUID is used, the signal is yet larger than that of circuit 2. This is mainly contributed by the larger shift in peak position as a result of the smaller biasing inductance.

4.2.4 Inductance measurement with circuit 4: Aggressive SQUID with 30pF resonance capacitor

Finally, the analysis was performed with circuit 4 (fig. 4-8) and the important results are summarized below.

Circuit 4			
	Bias	MIT	Delft
Signal size [Φ_o]	–	0.01	0.001
Flux Level [Φ_o]	0.67	0.68	0.671
f_o [MHz]	494.9	495.6	499.4
Δf_o [MHz]	–	0.7	4.5

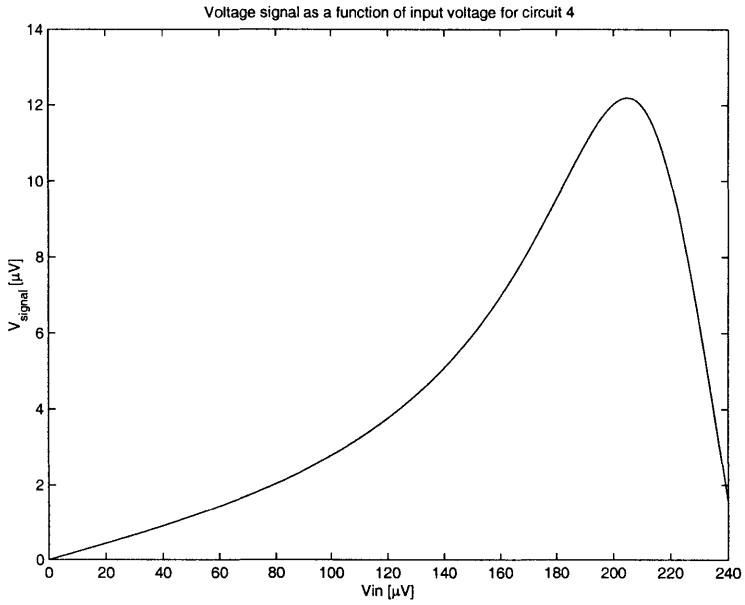

Figure 4-21: Voltage signal as a function of input voltage for circuit 4. The frequency bias is 475MHz. The optimal input voltage is $200\mu V$ yielding a voltage signal of $12.1\mu V$. Although this design uses an aggressive SQUID, the signal is comparable yet not signifcantly better than circuit 3 which uses a conservative SQUID. This is due to the fact that the Q of this circuit is smaller than that of circuit 3.

4.3 Schematics of RF electronics

The discussion so far has been mainly a presentation of the simulated results of the SQUID inductance measurement, and the conceptual ideas of the measurement procedures were emphasized. Before we end this chapter, we will briefly discuss how the voltage signal can be measured experimentally. The schematics of the RF electronics are shown in figure 4-22. Referring to the diagram, the amplitude of the single frequency RF source is denoted as V_{in}. The output voltage has the same frequency, but its amplitude depends on the transfer characteristics of the SQUID resonant circuit at that particular frequency, which in turn is sensitive to the qubit flux. The amplitude of this output voltage is expected to be very small, and the signal has to pass through a series of amplifiers. Finally, the AC output voltage is converted to a DC signal using a PIN diode. The DC level is proportional to the power of the original waveform. The qubit signal is detected as a difference in the DC voltage levels.

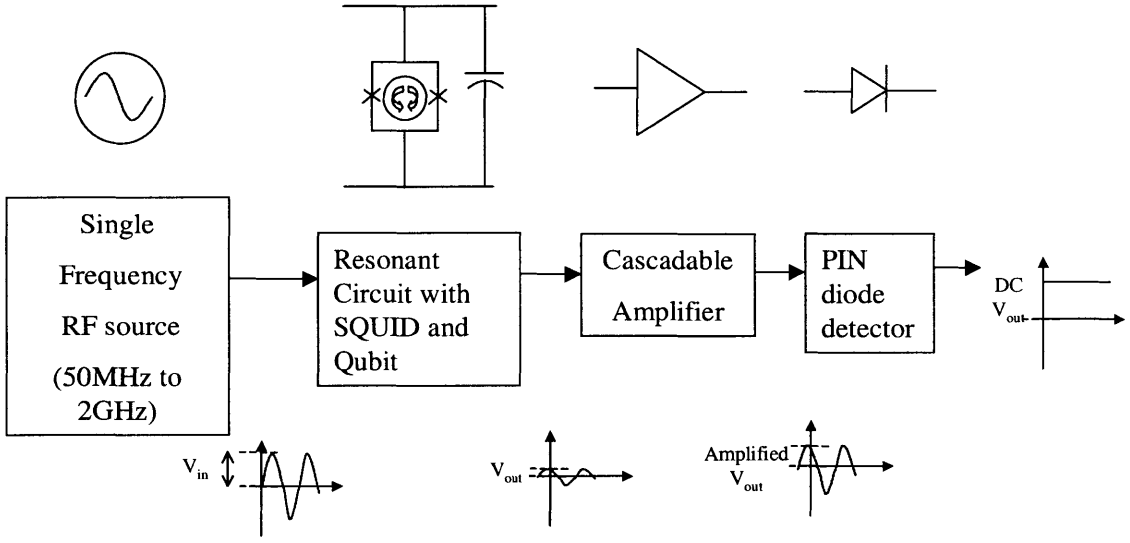

Figure 4-22: Schematics of RF electronics for measuring the voltage output.

4.3.1 Summary

The strategy of mapping the qubit flux signal to a difference in amplitude of the AC voltage output was presented. The voltage difference due to a flux signal of $0.01\Phi_o$ was calculated for each of the four on-chip designs and ranges from $2.4\mu V$ to $12.1\mu V$. The results are summarized in the following table. Keep in mind that when the qubit changes from one state to another, the overall flux difference will be $0.02\Phi_o$, and hence the voltage difference will be twice as large.

Summary of Voltage Signal Calculations						
	SQUID	$C_{res}[pF]$	$f_{bias}[MHz]$	$V_{in}[\mu V]$	$I_{L,AC}$	$V_{signal}[\mu V]$
Circuit 1	Con.	10	580	190	$0.15I_c$	2.4
Circuit 2	Agg.	10	570	175	$0.1I_c$	5.7
Circuit 3	Con.	100	475	210	$0.1I_c$	11.8
Circuit 4	Agg.	30	475	200	$0.1I_c$	12.1

Chapter 5

Decoherence Calculations of SQUID Inductance Measurement

Abstract

The relaxation and dephasing times of the qubit resulting from the on-chip SQUID inductance measurement circuits were calculated based on the spin-boson model. The effect of circuit design, mutual coupling, and the SQUID bias current on decoherence will be discussed. The idea of using the inductance measurement to measure the effect of the SQUID bias current experimentally will also be proposed.

5.1 Calculating Relaxation and Dephasing Times with Spin-boson Theory

In the previous chapter, we presented several circuits which were designed based on considerations for maximizing the signal size and sensitivity of the inductance measurement, as well as fabrication constraints. We will now analyze the decoherence of the qubit resulting from such measuring circuits. In particular, the relaxation and dephasing times will be calculated using the spin-boson theory.

The relaxation time determines how fast the qubit relaxes from a certain quantum state to its equilibrium state, based on the occupancy probability in each state given by the diagonal terms of the density matrix. The dephasing time determines how fast the qubit loses coherence information, i.e. when the off-diagonal elements of the density matrix goes to zero. As far as the measurement process is concerned, the relaxation time bears much more significance than the dephasing time, because it directly affects the measurement results. On the other hand, the fact that a qubit dephases and loses the coherence information only means it cannot be used for further computation, and is not a concern once the measurement process has started.

The spin-boson model estimates the relaxation time τ_r and dephasing time τ_ϕ by assuming the 2-level quantum system is coupled to some impedance $Z_t(\omega)$ described

by a bath of LC oscillators [13, 4]. The influence of the oscillator bath on the qubit is described by the *environmental spectral density function* $J(\omega)$. For the specific case of a measuring DC SQUID, $J(\omega)$ is given by [4]:

$$J(\omega) = \frac{(2\pi)^2}{\hbar\omega}(\frac{MI_p}{\Phi_o})^2 I_L^2 \tan^2\Phi \Re e[Z_t(\omega)] \tag{5.1}$$

where M is the mutual inductance between the SQUID and the qubit, I_p is the size of the persistent current, I_L is the bias current through the SQUID, Φ is the external flux bias, and $Z_t(\omega)$ is the total circuit impedance as a function of operating frequency. Note that Z_t is the impedance as seen by the qubit, and is different from the usual circuit impedance as seen by the source. The dimensionless factor $(\frac{MI_p}{\Phi_o})$ describes how strongly the qubit is coupled to the SQUID. As the coupling grows stronger, the spectral density $J(\omega)$ gets bigger in a quadratic fashion, and as will be seen later, leads to faster decoherence times.

Before introducing the expression for τ_r and τ_ϕ, we need to define some parameters for the qubit operation. We define the Hamiltonian of the two-level system as

$$H = \frac{\varepsilon}{2}\sigma_z + \frac{\Delta}{2}\sigma_x \tag{5.2}$$

where σ_z and σ_x are Pauli matrices, ε is the energy bias and Δ is the coupling parameter. The proposed operation point is to have $\varepsilon \approx 5\Delta$. The two energy eigenvalues of the system is

$$E_\pm = \pm\frac{1}{2}\sqrt{\varepsilon^2 + \Delta^2} \tag{5.3}$$

and the energy separation ν between the two states is given by $E_+ - E_-$:

$$\nu = \sqrt{\varepsilon^2 + \Delta^2} = \hbar\omega_{res} \tag{5.4}$$

Now we will introduce the relaxation rate, which is the inverse of the relaxation time. It is given by the expression:

$$\Gamma_r = \tau_r^{-1} = \frac{1}{2}(\frac{\Delta}{\nu})^2 J(\omega_{res}) \coth(\frac{\nu}{2k_BT}) \tag{5.5}$$

where ω_{res} is the resonance frequency range over which the qubit is operated, and is between 5 and 15GHz. The prefactor $\frac{\Delta}{\nu}$ is related to eqns. 5.2 and 5.4 above. Since $\nu = \hbar\omega_{res}$, the value of the prefactor should be a function of frequency as well. However over the qubit frequency range of 5-15GHz, the value is fairly constant, and for simplicity can be approximated by using $\varepsilon \approx 5\Delta$ which gives:

$$(\frac{\Delta}{\nu})^2 = \frac{1}{26} \tag{5.6}$$

$$(\frac{\varepsilon}{\nu})^2 = \frac{25}{26} \tag{5.7}$$

The dephasing rate is in turn given by the expression:

$$\Gamma_\phi = \tau_\phi^{-1} = \frac{\Gamma_r}{2} + (\frac{\varepsilon}{\nu})^2 \alpha 2\pi \frac{k_B T}{\hbar} \tag{5.8}$$

Even though the dephasing rate depends on the relaxation rate through the first term, it is actually dominated by the second term (especially α) which is much smaller. α is a dissipation factor determined by the slope of $J(\omega)$ at very low frequencies, and thus strongly depends on the circuit impedance at low frequencies:

$$\alpha = \lim_{\omega \to 0} \frac{J(\omega)}{2\pi\omega} \approx \frac{1}{2\pi} \frac{\partial J(\omega)}{\partial \omega} \tag{5.9}$$

5.2 Decoherence due to on-chip SQUID Inductance Experiments

We will now analyze the decoherence due to the SQUID inductance measurement based on the above theory. The calculations will mainly focus on the specific on-chip experiments that were presented in chapter 4.

5.2.1 Tapped-L circuit with 10pF resonance capacitor

Figure 5-1 corresponds to the circuit in fig.4-1. It is redrawn here across the ports as seen by the qubit for decoherence calculation purpose. The qubit is shown coupled to the SQUID which is modelled by the inductance L_J. The results from the calculations of $\Re e[Z_t(\omega)]$, $J(\omega)$, τ_r, and τ_ϕ are presented in figures 5-2 to 5-5.

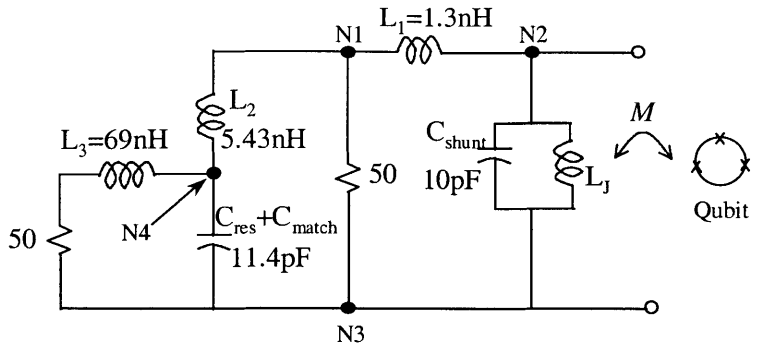

Figure 5-1: Tapped-L circuit redrawn across ports as seen by the qubit. The resonance capacitor C_{res} of 10pF is in parallel with the matching network capacitor C_{match} of 1.4pF. $L_J = 0.225$nH.

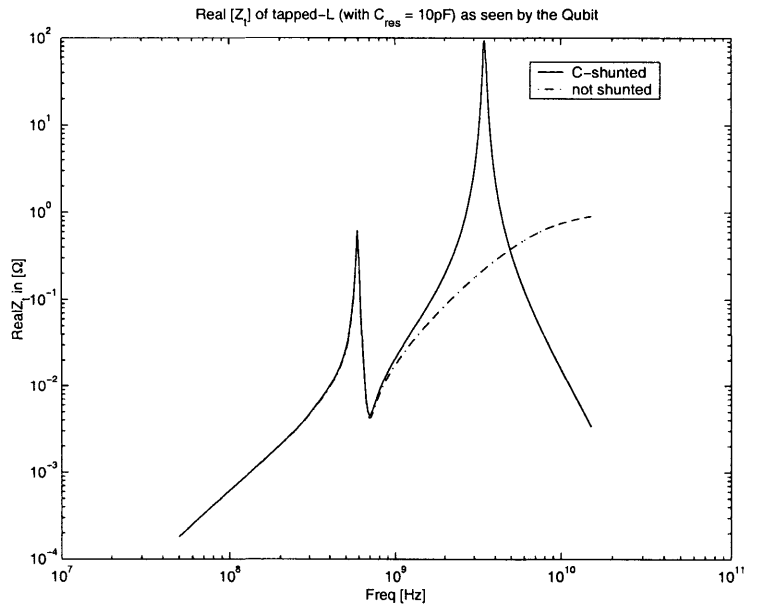

Figure 5-2: $Z_t(\omega)$ of the tapped-L circuit. The dashed line shows the case without the shunting capacitor and the solid line corresponds to the case when the SQUID is shunted with $C_{shunt} = 10$pF. For the non-shunted case, the impedance has an undesired 'tail' which levels off to a constant of $10^0\Omega(1\Omega)$ at high frequencies . Fortunately, the presence of the shunting capacitor has an effect of bringing the impedance down. The shunting capacitance was chosen to be large enough to bias the peak below the 5-15GHz range. The resultant peaks in the figure occur at 590MHz and 3.5GHz.

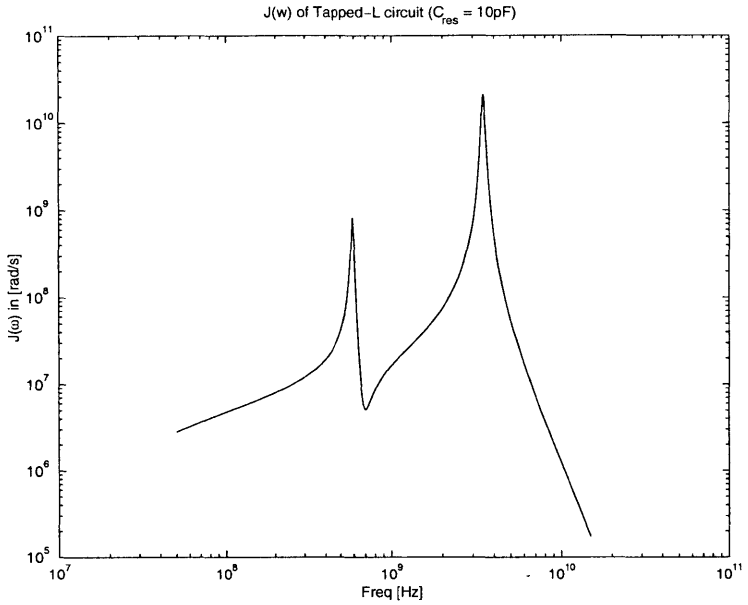

Figure 5-3: The spectral density $J(\omega)$. The parameters used were M = 8pH, I_p = 500nA, T =30mK, $I_L = 0.3I_c$, $I_c = 3.63\mu A$, $\Phi = 0.67\Phi_o$.

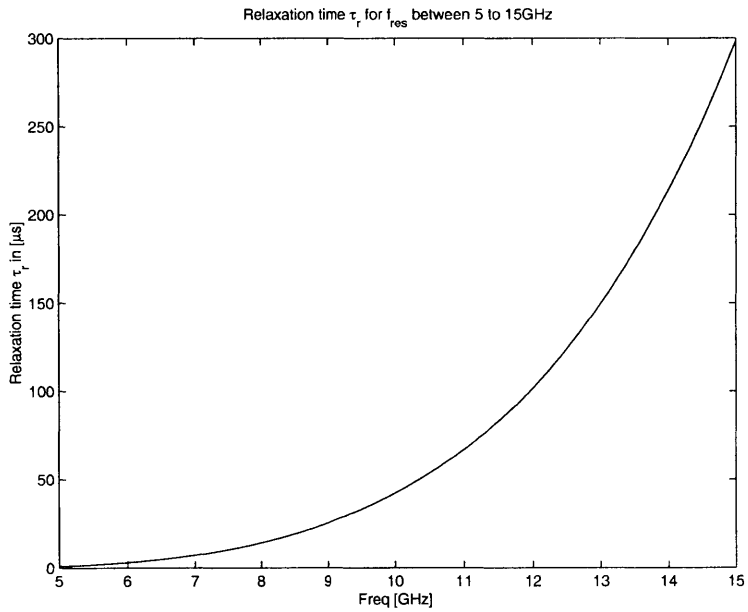

Figure 5-4: Relaxation time τ_r for the resonant frequency range of 5-15GHz. $(\frac{\Delta}{\nu})^2$ was assumed to be constant and equal to $\frac{1}{25}$. The plot indicates a trend of longer relaxation time as one moves further away from the resonant peaks, especially the second peak due to the shunting capacitor since it is at a much higher frequency. $\tau_r \approx 42\mu s$ at 10GHz.

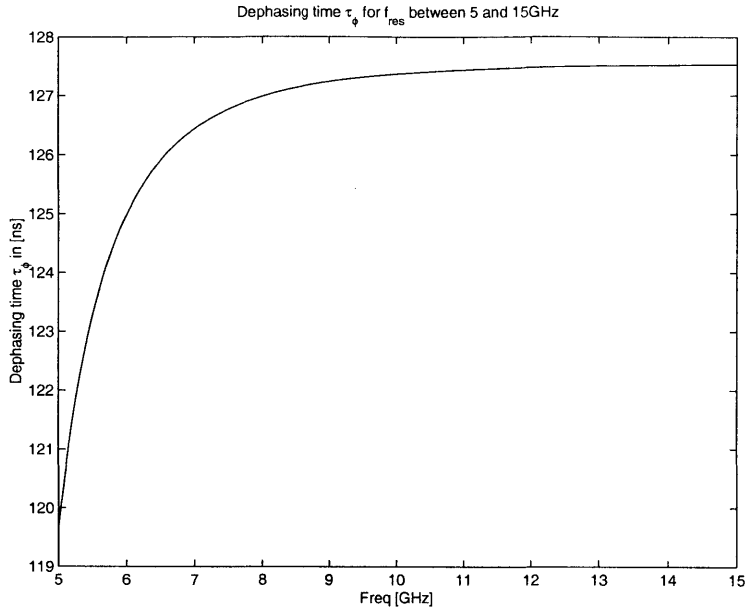

Figure 5-5: Dephasing time τ_ϕ for the resonant frequency range of 5-15GHz. $\alpha = 0.0003$, $(\frac{\varepsilon}{\nu})^2$ was assumed to be $\frac{25}{26}$. Unlike the relaxation time, it has a trend of levelling off. $\tau_\phi \approx 127ns$ at 10GHz

Effect of coupling ($C_{res} = 10pF$)

As mentioned before, the strength of the qubit-SQUID coupling has a strong effect on the decoherence values. To illustrate this further, we have repeated the above calculations with a combination of different M and I_p values. Case 1 is based on the parameters from the Delft experiments, while case 4 is based on the current parameters in our experiments.

	M [pH]	I_p [nA]	slope $\lim_{\omega\to 0} \frac{\partial J(\omega)}{\partial \omega}$	α	τ_r@10GHz	τ_ϕ@10GHz
Case 1	8	500	0.002	0.0003	$42\mu s$	127ns
Case 2	30.5	500	0.03	0.0048	$2.9\mu s$	8.8ns
Case 3	8	915	0.007	0.0011	$10.3\mu s$	38ns
Case 4	30.5	915	0.10	0.0161	$0.86\mu s$	2.6ns

Effect of bias current through the SQUID ($C_{res} = 10pF$)

One of the main advantages of the SQUID inductance measurement scheme is the capability to vary the bias current through the SQUID. As discussed in chapter 1, decoherence calculations for the switching current method have showed that the level of decoherence increases with the amount of bias current. This can also be easily seen from the equation for $J(\omega)$ which is proportional to I^2_{SQUID}. The inductance measurement therefore has the potential to study the effect of the bias current on

decoherence time experimentally. In figures 5-6 and 5-7, the dependence of the decoherence times on the bias current is shown.

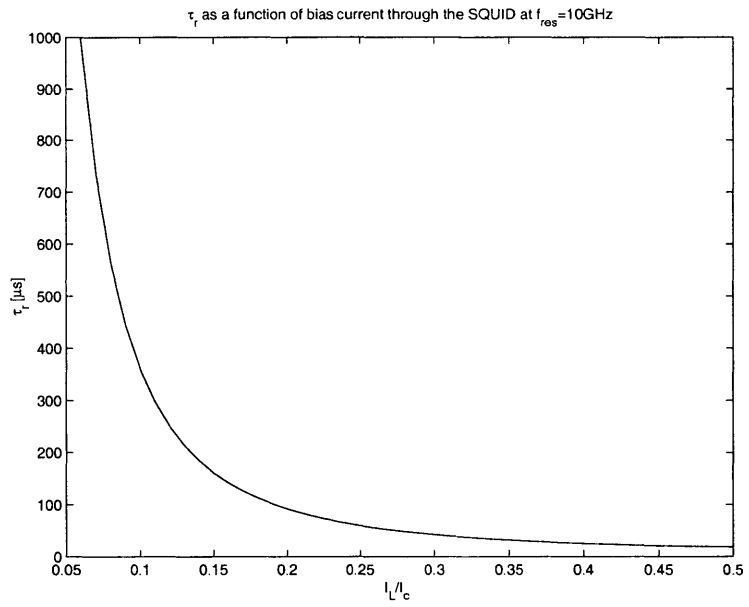

Figure 5-6: Relaxation time as a function of bias current through the SQUID. The resonant frequency is set at 10GHz, M = 8pH, I_p = 500nA. I_c here equals $2I_{co}$ and is the critical current when Φ is zero. The proposed operating point is to have $\Phi = 0.67\Phi_o$, and thus the actual critical current of the SQUID is suppressed to $2I_{co}|\cos\pi\frac{\Phi}{\Phi_o}| \approx 0.5I_c$. Currents above $0.5I_c$ is no longer along the supercurrent branch and are therefore not plotted. The plot shows clearly that the relaxation time is longer as one moves to lower biasing current.

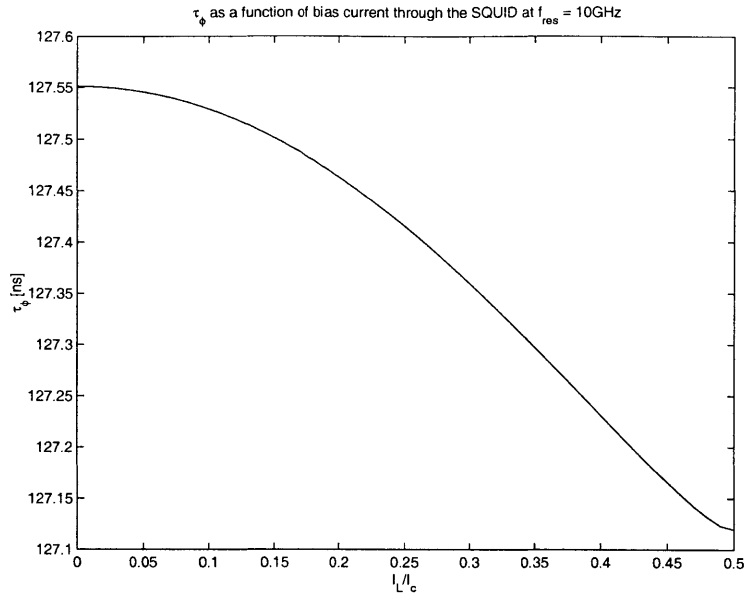

Figure 5-7: Dephasing time as a function of bias current through the SQUID. The resonant frequency is set at 10GHz, M = 8pH, I_p = 500nA. The plot shows that the dephasing time does not vary much with biasing current.

5.2.2 Tapped-L circuit with 100pF resonance capacitor

The analysis was then performed for the tapped-L circuit with a resonance capacitor of 100pF(circuit 3). As expected, the results are very similar to the C_{res} = 10pF case, and are summarized in the following figures.

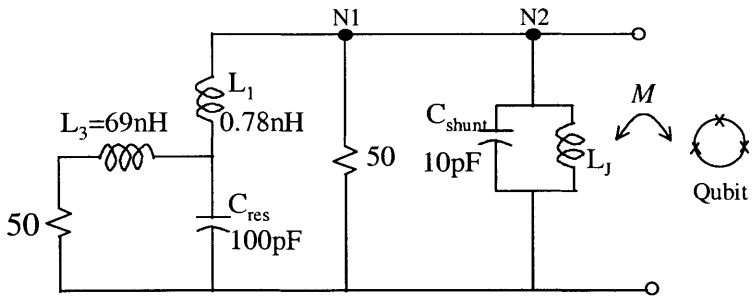

Figure 5-8: Tapped-L circuit redrawn across ports as seen by the qubit. Only the resonance capacitor of 100pF is shown, for the capacitor of the L-matching is a lot smaller (1.4pF) and thus ignored. $L_J = 0.225$nH.

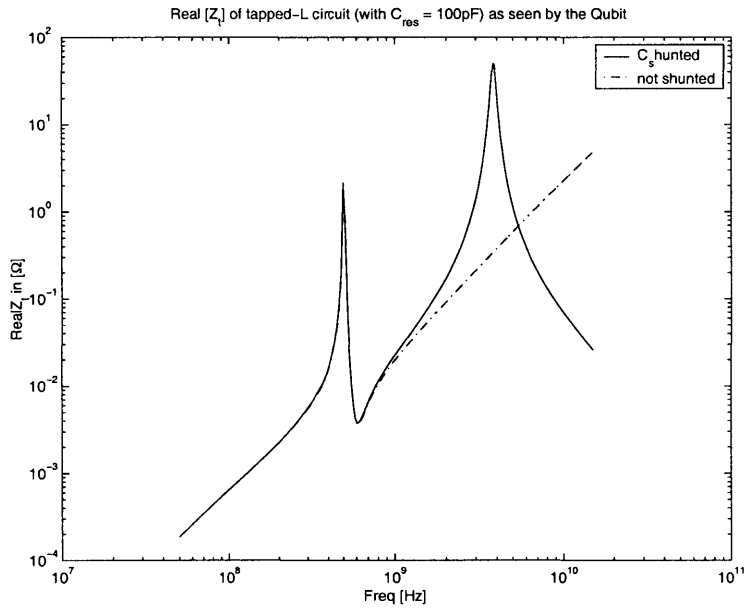

Figure 5-9: $Z_t(\omega)$ of the tapped-L circuit. The dashed line shows the case without the shunting capacitor and the solid line corresponds to the case when the SQUID is shunted with $C_{shunt} = 10$pF. The peaks occur at 496MHz and 3.5GHz. The characteristics have two major differences from the previous design with C_{res} of 10pF. Firstly, the first peak has a larger magnitude and is a signature of a higher Q associated with a larger C_{res}. Secondly, for the non-shunted case, the 'tail' levels off to 50Ω at high frequencies.

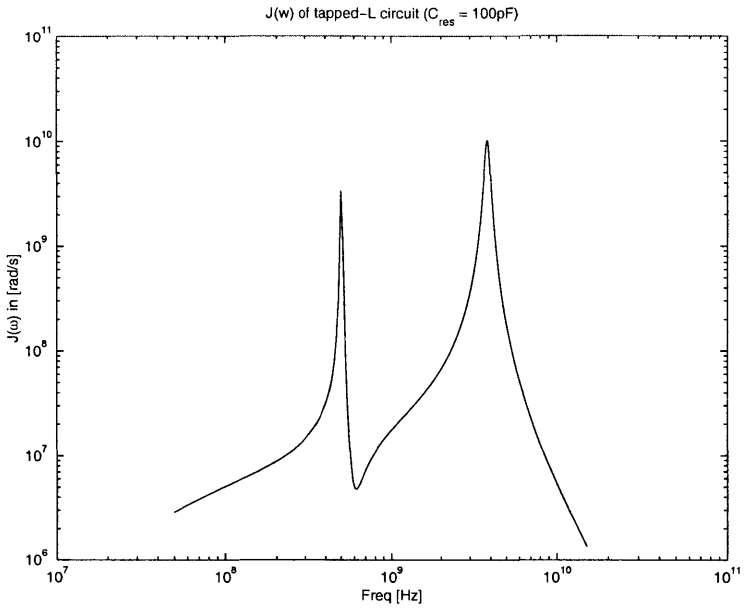

Figure 5-10: The spectral density $J(\omega)$. The parameters used were same as the $C_{res} = 10pF$ case, with M = 8pH, I_p = 500nA, T =30mK, $I_L = 0.3I_c$, $I_c = 3.63\mu A$, $\Phi = 0.67\Phi_o$.

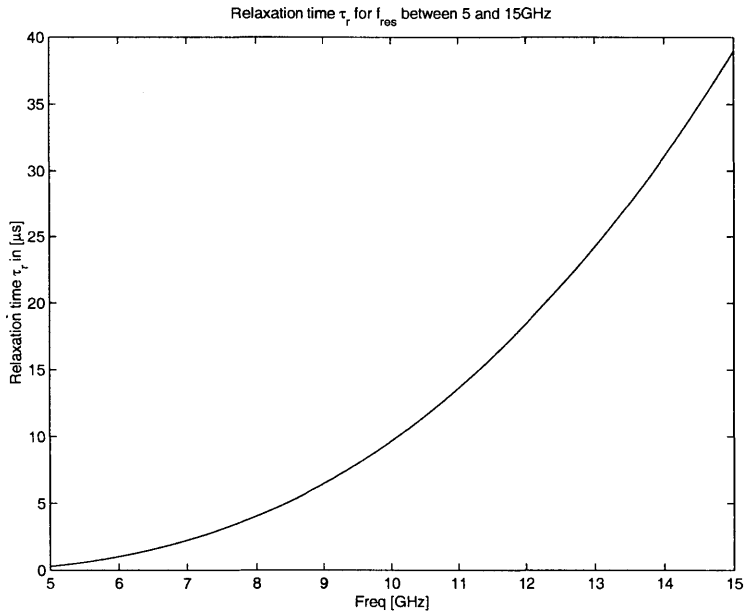

Figure 5-11: Relaxation time τ_r for the resonant frequency range of 5-15GHz. In general, the relaxation times are shorter compared to the C_{res} = 100pF case. $\tau_r \approx 9.4\mu s$ at 10GHz

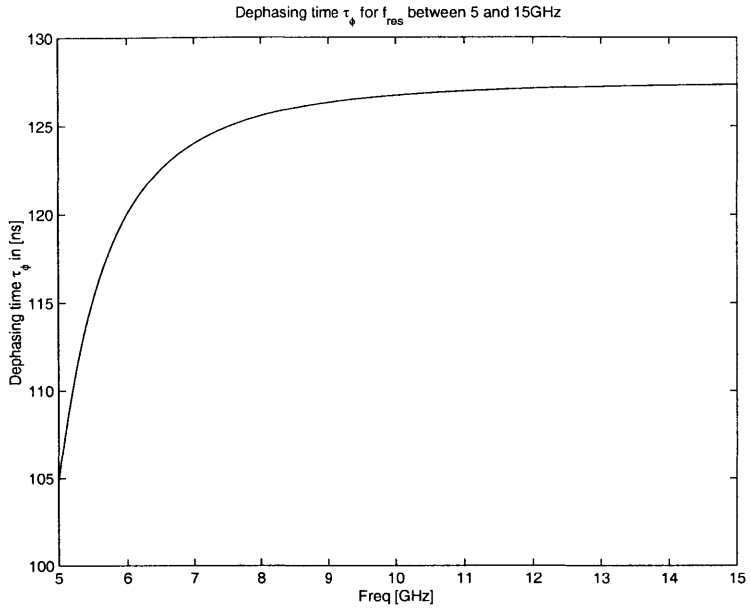

Figure 5-12: Dephasing time τ_ϕ for the resonant frequency range of 5-15GHz. α is still the same as the C_{res} being 10pF case, and is equal to 0.0003. Since the dephasing time is mainly dominated by α, it is also comparable to the 10pF case as well.

Effect of coupling ($C_{res} = 100pF$)

The following table summarizes the decoherence calculations for the tapped-L circuit with C_{res} = 100pF for different coupling parameters. The relaxation times are about 4 times shorter than the earlier circuit design with a smaller C_{res} of 10pF. The dephasing times, on the other hand, are exactly the same.

	M [pH]	I_p [nA]	slope $\lim_{\omega\to 0} \frac{\partial J(\omega)}{\partial \omega}$	α	τ_r@10GHz	τ_ϕ@10GHz
Case 1	8	500	0.002	0.0003	$9.4\mu s$	127ns
Case 2	30.5	500	0.03	0.0048	$0.62\mu s$	8.8ns
Case 3	8	915	0.007	0.0011	$2.7\mu s$	38ns
Case 4	30.5	915	0.10	0.0161	$0.2\mu s$	2.6ns

Effect of bias current through the SQUID ($C_{res} = 100pF$)

The dependence of the decoherence times on the bias current through the SQUID is shown in figures 5-13 and 5-14.

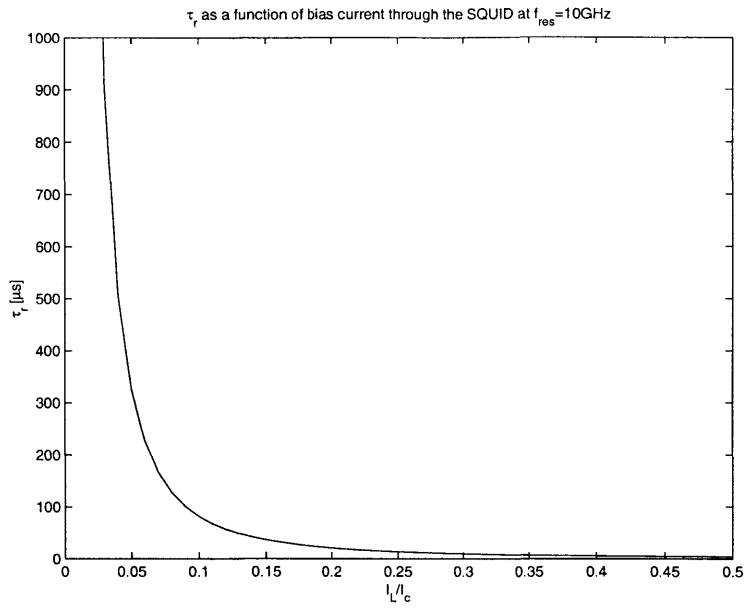

Figure 5-13: Relaxation time as a function of bias current through the SQUID. The resonant frequency is set at 10GHz, M = 8pH, I_p = 500nA, $\Phi = 0.67\Phi_o$. The x-axis spans the supercurrent branch.

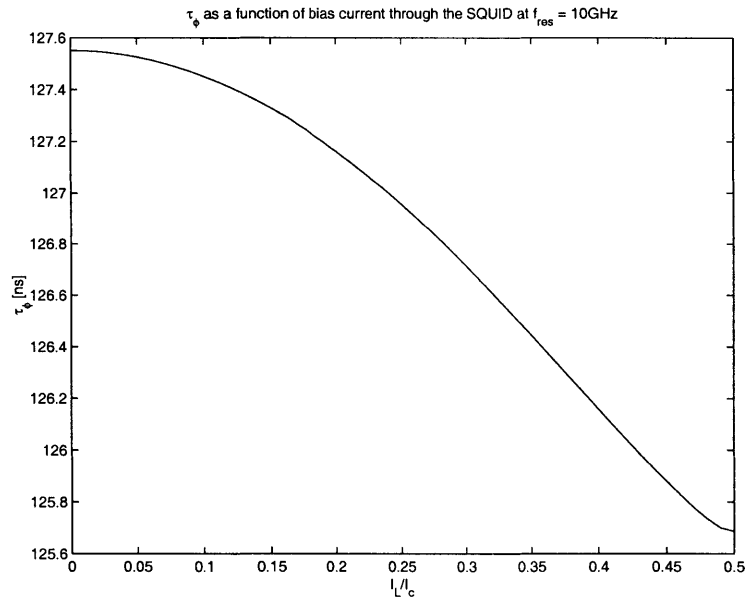

Figure 5-14: Dephasing time as a function of bias current through the SQUID. The resonant frequency is set at 10GHz, M = 8pH, I_p = 500nA, $\Phi = 0.67\Phi_o$. As in the previous case with C_{res}= 10pF, the dephasing time is fairly constant over the whole range.

5.3 Discussion

Two inductance measurement circuits were analyzed for their effects on the decoherence of the qubit. For the first tapped-L design with a 10pF resonance capacitor, the relaxation times at 10GHz are calculated to be 0.86 to 42μs depending on the qubit-SQUID coupling. The second design with a 100pF resonance capacitor has relaxation times between 0.2 to 9.4μs at 10GHz. The difference here originates from the circuit design, but more thought is needed to account for the exact cause. One observation was that as the biasing inductance (L_2 in figure 5-1) decreased, the relaxation time increased accordingly. In any case, the two sets of relaxation values are of the same order and the difference can be accepted. As for the dephasing times, both designs have values between 2.6 to 127ns depending on the coupling.

It is reasonable to compare our results with that for the switching current method [4]. For the conditions of I_{squid} = 120nA, I_c = 200nA, M=8pH, and I_p = 500nA, the relaxation time τ_r for the switching current case was between $10^3\mu s$ at 5GHz to $10^5\mu s$ at 15GHz, while the dephasing time is fairly constant at 70ns over the frequency range. However, one should be aware that these calculations were not done for higher bias values for I_{squid}, and that the actual effect on decoherence immediately before the switching action was not included. Nevertheless, this suggests that there is certainly room for improving the inductance measurement circuits as far as decoherence is concerned, especially that the circuits were designed so far to mainly optimize the resonant characteristics and sensitivity for the measurements.

The main constraint for not achieving longer relaxation times at this point is in fact not so much due to the principles of the inductance measurement, but rather due to the shunting capacitor across the SQUID. The shunting capacitor was originally inserted to narrow the distribution of the measured results. It also has a significance of relieving the electro-static discharge (ESD) problems with the junctions. However, the shunting capacitor and the Josephson inductance of the SQUID introduces an additional resonant peak; operating the qubit near the resonant frequency regime leads to extremely short decoherence times. As a result, the shunting capacitance has to be carefully chosen to avoid causing the resonant peak to occur in the qubit frequency range (5-15GHz). From the calculated results, the shunting capacitor is recommended to be at least 10pF, preferably larger, at which case the resonant peak is at about 3.5GHz. At Delft, the resonant peak is biased at 500MHz and significantly away from the qubit frequency, hence the much improved relaxation time. However, this poses a new concern that the peak now falls right into the SQUID inductance frequency range. A possible alternative is to keep the resonant peak still near 3.5GHz, but design the peak to be much sharper (with a higher Q). In this way, the amplitude past the resonant peak decays faster and will have less effect in the qubit frequency range. This can be achieved by raising the resistance in the branch N1-N3 in figure 5-1. For instance, when R is raised from 50Ω to 2$k\Omega$, τ_r increases from 40μs to 400μs. However, since the voltage output is always measured across a 50Ω input resistance of the amplifier, the voltage signal will be significantly reduced by the voltage divider

ratio of $\frac{50}{2k}$ and may not be desired.

There are some additional issues that are worth special attention. Firstly, referring to the dotted line of figure 5-2, the real impedance of the circuit without the shunting capacitor has a 'tail' that climbs up at high frequencies. This is because in the higher frequency regime past the resonance, the impedance of L_2 of figure 5-1 starts to dominate and the current would be forced to enter the branch N1-N3 rather than N1-N4. N1-N3 has purely real impedance, consequently the real part of $Z_t(\omega)$ increases. Fortunately, once the SQUID is capacitively shunted, the 'tail' can be suppressed by the falling edge of the resonant peak introduced by the shunting capacitor. Thus this turns out not to be a concern.

In addition, the coupling between the qubit and the SQUID has a significant role on decoherence. This is well expected and agrees with the dilemma that a strong coupling between the detector and the qubit yields a strong signal but also introduces severe decoherence on the qubit. The first coupling parameter is the mutual inductance M between the SQUID and the qubit. It mainly depends on the geometric loop sizes and the proximity between the structures. For the on-chip designs at MIT, M is about 30pH. While at Delft, the dimensions of the SQUID and the qubit are both smaller and correspond to M = 8pH. The second coupling parameter is the size of the persistent current in the qubit loop I_p. This is mainly determined by the critical current of the junctions. It is about 915nA in our case and 500nA for Delft. Consequently, the coupling parameters at MIT yield a larger signal, yet the relaxation time is about 50 times shorter.

Finally, the inductance measurement has the flexibility to vary the SQUID bias current while the switching current method does not. Therefore, the inductance measurement can serve as a valuable tool to study the effect of the bias current on decoherence experimentally. One may be concerned that since the optimal signal of the inductance measurement relies critically on the bias current, and so as one gradually varies the current away from the optimal point, the signal will inevitably suffer. Fortunately, the operation relies mainly on the amplitude of the AC bias and less so on the DC bias. So far as the SQUID is kept in the supercurrent branch, one may use the DC current bias as a knob to measure the corresponding decoherence times. Unwanted issues such as the non-linear effects of the Josephson inductance may come into play, but should not affect the principles of the operation.

Chapter 6

Conclusion and Future Work

In this thesis, we have presented a way of measuring the state of the superconducting persistent current qubit by operating the SQUID magnetometer as a flux-sensitive inductor. Unlike the preceding switching current method, the current through the SQUID can now be biased significantly below the critical current level. Prototype resonant circuits were made with chip components on printed circuit boards. The resonant testing at room temperature with a network analyzer enhanced our understanding of the parasitics and confirmed the reliability of the impedance matching design and the tapped-L impedance transformation. Four high-Q on-chip circuits were designed with optimizing the signal of the inductance measurement in mind. These circuits will soon be in fabrication and tested. The operating procedures have been carefully thought through with the specific circuit parameters. Optimal biasing points for the external magnetic flux, DC bias current and AC bias current through the SQUID were proposed. Despite the extremely small value of the SQUID Josephson inductance, the resulting voltage signal from the qubit ranges from 2 to 12 μV depending on the circuit, and is large enough to be measured. Calculations of the decoherence times for the specific circuits were also performed, and the results suggested that the relaxation times are on the order of 1 to 50 μs depending on the strength of coupling between the qubit and the SQUID.

This thesis laid the foundation for experimentally implementing the SQUID inductance measurement. It has taken the work to a point where several significant experiments are ready to be carried out in the near future. Preparation for RF measurements at 4 kelvin has started with the setup of the co-axial lines and the installation of a new sample stage on the cryostat. The current task involves building the RF electronics to replace the functionality of the network analyzer. Off-chip inductance measurements with a SQUID and chip components is also well underway; this will facilitate the future testing of the on-chip experiments. Not only this new measurement scheme provides an improved way to detect the qubit state, it also has the promise of studying the effect of the biasing conditions on decoherence. The prospect of the SQUID inductance measurement looks very promising in the years to come.

Appendix A

Copper powder Filters

Copper powder filters are microwave filters used in cryogenic experiments especially those involving Josephson junctions and SETs [14]. These passive filters serve to eliminate electromagnetic noise introduced through the lead wires from the high-temperature part of the experimental setup. A general description of the filters and the making procedures are presented below. With reference to some literature, the effect of varying the components such as the material of the inner wire, the type of powder and the grain size will also be discussed.

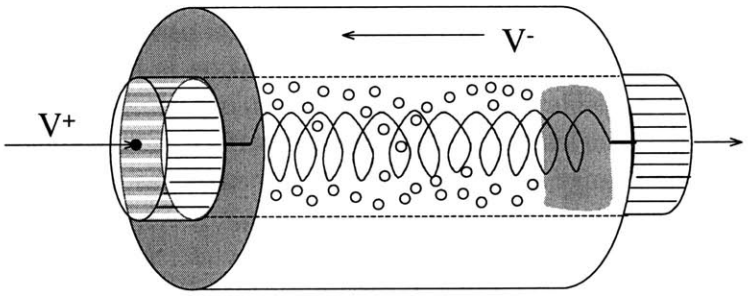

Figure A-1: Cross section of a copper powder filter. The center wire is wound into a coil and acts as the inner conductor. The copper tube housing acts as the outer conductor. The SMA connectors are press-fit into the copper tube at both ends. The powder fills up the space inbetween and can be thought of a damping material for the electromagnetic signal. A small amount of epoxy is added at the end to improve the thermal property at low temperature.

The cross section of a typical powder filter is shown in figure A-1. The filter is made from an insulated wire wound into a coil. The coil is then housed inside a copper tube filled with metallic powder made from copper or stainless steel. The insulation of the wire is stripped off at both ends, and each end is attached to a SMA connector. The connectors are then press fit into the tube. The tube acts as an outer conductor while the wire is the inner conductor. The powder can be thought of as a damping material inbetween. A small amount of epoxy is added to the copper powder as a

thermal anchor at low temperature. For reference, the complete procedures are listed at the end of this section.

The filter essentially acts as a low-pass network as shown in figure A-2. The capacitance is contributed by the natural oxide layer on the surface of the grain, and the big resistance R is the sheet resistance due to the skin depth effect. Moreover, L is the inductance of the wire and r is the resistance of the wire and is very small.

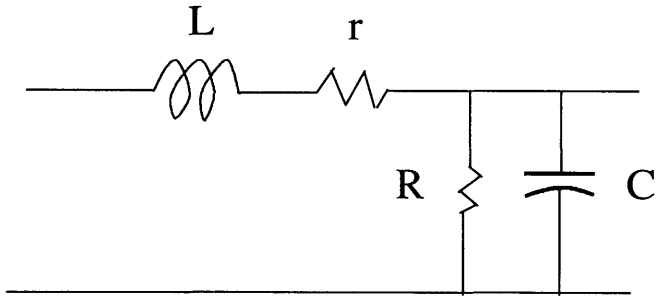

Figure A-2: Low pass model of the powder filter.

The attenuation property of the filters were studied by varying the component sizes [15]. In summary, it was found that stainless steel powder has a stronger attenuation than copper powder. Moreover, the attenuation is larger for a grain size of $30\mu m$ than $1\mu m$. A possible reason was that the more compact packing associated with the smaller grain size leads to a less effective surface area of the oxide layer. The attenuation has little change when the inner copper wire was replaced by a superconducting wire, but depends on the length of the wire.

Figure A-3 shows the transfer characteristics of the powder filters made in our group. The inner wire was 1m long. The powder was made from stainless steel and of 325 mesh size. The epoxy was BIPAX Tra-bond BA-2115. The solid line shows the data from a filter made with a magnet wire of copper core (Belden 8083, AWG 34), and the dotted line corresponds to a manganin wire (5mils OD). Both materials show similar characteristics. The attenuation reaches -3dB at 60MHz and -20dB by 1GHz.

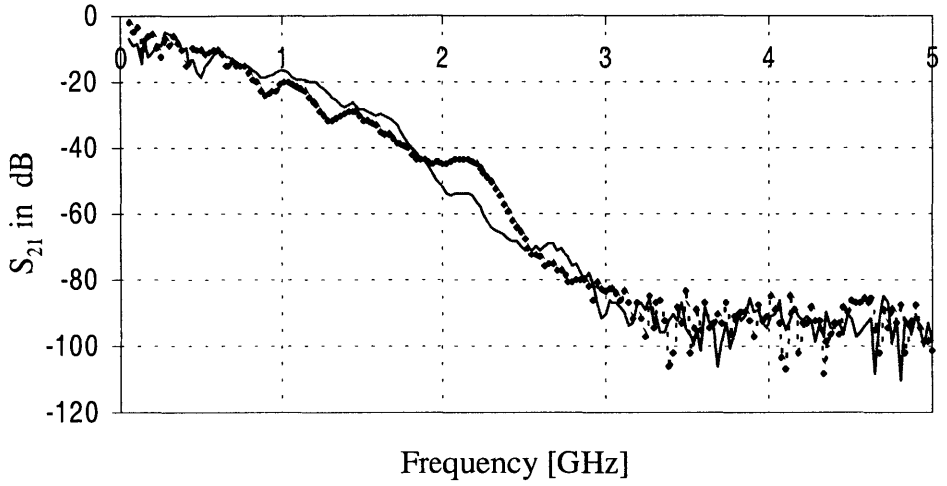

Figure A-3: Attenuation characteristics of the powder filters. The solid line shows data for a copper inner wire, and the dotted line corresponds to a manganin wire. The attenuation reaches -3dB at 60MHz and -20dB by 1GHz.

Procedures to make a copper powder filter

A. Copper Tube:

1. Start with a copper cylinder or a specific shape designed to fit on the sample stage.

2. Drill a hole through the center of the cylinder in two steps. Use a 1st drill bit of size no. 12, then use a 2nd drill bit of size 13/64". The size of the hole has to be fairly accurate in order for the SMA connectors (Johnson's components 528-1970) to press fit.

B. Filter:

1. Cut a piece of insulated copper wire (Belden 8083) about 1 meter long.

2. Wind the wire into a coil by wrapping it tightly around a rod of 0.125" O.D. or a wooden stick e.g. Q-tip.

3. Strip about 5mm of the insulation off at both ends with sand paper or a razor blade.

4. Solder one stripped end (exposed copper) to the center gold conductor of a SMA connector.

5. Slightly wind the remaining exposed length tightly around the center conductor.

6. Squeeze some Duno Cement all around the solder connection to insulate the wire and the center conductor from the outside. This is particularly important to avoid shorting the filter when the tube is later filled with metallic powder.

7. Allow the Duno Cement to dry for 15 mins.

8. Add a drop of epoxy (Tra-Bond 2115) on the hardened cement to ensure complete insulation.

9. Allow the epoxy to dry for 15 mins.

10. Pass the coil through the hole of the copper tube prepared in part A.

11. Press fit the SMA connector at one end of the copper tube. Use a vice for press-fitting. Put some soft insulation (e.g. plastic block) between the vice and the connector to avoid damaging the connector. Make sure the coil is kept inside the tube while press-fitting to avoid damaging the coil. It may be useful to put some scotch tape to seal the other end of the hole so that the coil would not stick out on the other end.

12. After the connector is press-fit in the copper tube, remove the scotch tape, but use a finger to keep the coil in the hole.

13. Pick out the end of the stripped wire and keep it outside the hole.

14. Carefully use a micro-spoon to fill the hole with powder (Alfa Aesar 325 mesh, type 315-L).

15. Gently shake the tube occasionally to facilitate powder to settle. Fill the tube until 1cm below the top.

16. Add 1 to 2 drops of epoxy on top of the powder.

17. Wait for 15 mins for powder and epoxy mixture to settle. Add more powder and then epoxy if room permits. But remember to leave room for press-fitting the other SMA connector.

18. Partially cover the hole with scotch tape and let dry overnight.

19. On the next day, solder the remaining stripped end to the second SMA connector. Insulate with Duno Cement and epoxy as steps 6-8.

20. Press-fit the connector into the tube as step 11.

21. Check open/short of filter with a digital multimeter. The filter should be short when tested at the 2 ends of the inner SMA conductors, and open between the SMA inner conductors and the outer copper tube.

22. Filter is completed. Measure characteristics with network analyzer.

Remarks: Powder filters are made with SMA connectors so that the transfer characteristics can be tested with a network analyzer. Beyond the testing stage, actual filters are soldered to DC pin connectors at both ends. The DC pin connectors have been home-made with a short piece (about 1cm) of thick bare copper wire of 0.144" diameter (e.g. manufactured by Malin Co.) inserted through a short teflon tube (plastic plug). The tube can be made by drilling a 0.158" (slightly bigger than wire diameter) hole through the center of a teflon rod.

Manufacturers/Suppliers for Parts

- Insulated Copper Wire
  Manufacturer: Belden
  Part no: 8083

- Stainless Steel Powder
  Manufacturer: Alfa Aesar
  Specs: 325 mesh type 316-L

- Epoxy
  Manufacturer: Tra-Con
  Part no: BIPAX Tra-bond BA 2115

- SMA Connectors
  Manufacturer: Johnson's Components
  Distributer: Allied Electronics, 205 E. Central St., STE 10, Franklin, MA 02038.
  Tel: (508) 384-0400
  Manufacturer part no: 528-1970

Appendix B

Spiral Inductors

Some useful strategies for designing spiral inductors for on-chip circuits are presented based on [16, 17].

Figure B-1 shows a simple model of a spiral inductor. Other than the inductance L_s, there are also some parasitic capacitance C_s and C_{ox}. The overlap between the spiral and the overpass causes unwanted direct capacitive coupling between the two terminals of the inductor, and this is represented by C_s. The oxide capacitance between the spiral and the silicon substrate is modelled by C_{ox}. Note that there is no resistance associated with the Nb wire because the material is superconducting at 4K.

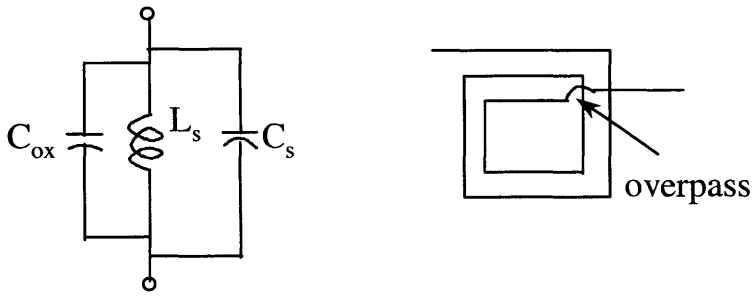

Figure B-1: Simple model of a spiral inductor(left) and the illustration of the overpass(right)

The overall inductance L_s is contributed partly by the self-inductance of each wire segment but mainly by the positive and negative mutual inductances between all possible pairs. Wires that are perpendicular to each other have no mutual coupling since their magnetic flux are not linked. The coupling is positive if the currents in the two wires are in the same direction and negative for opposite currents. Typically, the inter-winding spacing is either equal to or smaller than the width of the wire. The spiral inductors on QC4 were chosen to have both equal $1\mu m$. Smaller spacing improves the magnetic coupling and reduces the area of the spiral. A large spacing is only desired to reduce the interwinding capacitance, which is usually dominated by

the overpass capacitance anyway. In addition, it is usually preferred to leave as much space in the center of the spiral as possible. A spiral that is fully occupied towards the center has smaller inductance because the innermost turns in the center region contribute to more negative mutual inductance.

The performance of the spiral inductor is measured by its Q. The reduction of Q is caused by unwanted effects such as substrate loss and self-resonance. The self-resonant frequency is given by:

$$f_{os,spiral} = \frac{1}{\sqrt{L_s \times (C_s + C_{ox})}} \tag{B.1}$$

In addition, one has to make sure that the total length of the spiral is much shorter than the wavelength, so that it can still be considered as a lumped element. This is confirmed for the inductors on QC4 since the operating wavelength is about 60cm.

Bibliography

[1] J. E. Mooij, T. P. Orlando, L. Levitov, L. Tian, C. H. van der Wal, and S. Lloyd. Josephson persistent-current qubit. *Science*, 285, August 1999.

[2] T. P. Orlando, J. E. Mooij, L. Tian, C. H. van der Wal, L. S. Levitov, S. Lloyd, and J. J. Mazo. Superconducting persistent-current qubit. *Physical Review B*, 60(22), 1999.

[3] Caspar H. van der Wal, A. C. J. ter Haar, F. K. Wilhelm, R. N. Schouten, C. J. P. M. Harmans, T. P. Orlando, S. Lloyd, and J. E. Mooij. Quantum superposition of macroscopic persistent-current states. *Science*, 290, October 2000.

[4] Caspar H. van der Wal. *Quantum Superpositions of Persistent Josephson Currents*. PhD thesis, TU Delft University, the Netherlands, 2001.

[5] J. M. Martinis, S. W. Nam, J. Aumentado, and C. Urbina. Observation of rabi oscillations in large area josephson junctions. In *ASC Conference Proceedings*, 2002.

[6] J. R. Friedman, V. Patel, W. Chen, S. K. Tolpygo, and J. E. Lukens. Quantum superposition of distinct macroscopic states. *Nature*, 406:43, 2000.

[7] Kees Harmans. Measuring/interrogating a qubit magnetic state employing a dc-squid as a flux-sensitive inductor, August 2000.

[8] Andrew S. Kuziemko. A computer simulation of the effect of an alternating current on a squid. Bachelor thesis, Massachusetts Institute of Technology, 2002.

[9] Christopher Bowick. *RF Circuit Design*. Butterworth-Heinemann, 1998.

[10] Rainee N. Simons. *Coplanar Waveguide Circuits, Components, and Systems*. John-Wiley and Sons Inc., 2001.

[11] David M. Pozar. *Microwave Engineering*. John-Wiley and Sons Inc., 1997.

[12] Cam Nguyen. *Analysis Methods for RF, Microwave, and Millimeter-Wave Planar Transmission Line*. John-Wiley and Sons Inc., 2000.

[13] Lin Tian, Seth Lloyd, and T. P. Orlando. Decoherence and relaxation of a superconducting quantum bit during measurement. *Physical Review B*, 65(14), 2002.

[14] J. M. Martinis, M. H. Devoret, and J. Clarke. Experimental tests for the quantum behavior of a macroscopic degree of freedom: The phase difference across a josephson junction. *Physical Review B*, 35(10), 1987.

[15] A. Fukushima, A. Sato, A. Iwasa, Y. Nakamura, T. Komatsuzaki, and Y. Sakamoto. Attenuation of microwave filters for single-electron tunneling experiments. *IEEE Transaction on Instrumentation and Measurement*, 46(2), 1997.

[16] S. S. Mohan, M. del Mar Hershenson, S. P. Boyd, and T. H. Lee. Simple accurate expressions for planar spiral inductances. *IEEE Journal of Solid-state circuits*, 34(10), October 1999.

[17] C. Patrick Yue and S. Simon Wong. Design strategy of on-chip inductors for highly integrated rf systems. In *IEEE 36th Design Automation Conference Proceedings*, page 982, 1999.

[18] James W. Nilsson. *Electric Circuits.* Addison-Wesley, 1993.

[19] Terry P. Orlando and Kevin A. Delin. *Foundations of Applied Superconductivity.* Addison-Wesley, 1991.

[20] Theodore Van Duzer and Charles W. Turner. *Principles of Superconductive Devices and Circuits.* Prentice Hall, 1999.

[21] Alan M. Kadin. *Introduction to Superconducting Circuits.* John-Wiley and Sons Inc., 1999.

[22] Antonio Barone and Gianfranco Parerno. *Physics and Applications of Josephson Effect.* John-Wiley and Sons Inc., 1982.

[23] Jan Axelson. *Making Printed Circuit Boards.* McGraw-Hill, Inc., 1993.

[24] Robert A. White. *Spectrum and network measurements.* Prentice-Hall, Inc., 1991.

[25] E. Il'ichev, Th. Wagner, L. Fritzsch, J. Kunert, V. Schultze, T. May, and H. E. Hoenig. Characterization of superconducting structures designed for qubit realizations. *Applied Physics Letters*, 80(22), 2002.

[26] E. Il'ichev, V. Zakosarenko, L. Fritzsch, R. Stolz, H. E. Hoenig, H. G. Meyer, M. Götz, A. B. Zorin, V. V. Khanin, A. B. Pavolotsky, and J. Niemeyer. Radio-frequency based monitoring of small supercurrents. *Review of Scientific Instruments*, 2001.

[27] Y. Nakamura, C. D. Chen, and J. S. Tsai. Spectroscopy of energy-level splitting between two macroscopic quantum states of charge coherently superimposed by josephson coupling. *Physical Review Letters*, 1997.

[28] Y. Nakamura, Y. A. Pashkin, and J. S. Tsai. Coherent control of macroscopic quantum states in a single-cooper-pair box. *Nature*, 398, 1999.

[29] Y. Nakamura, Y. A. Pashkin, and J. S. Tsai. Rabi oscillations in a josephson-junction charge two-level system. *Physical Review Letters*, 87(24), 2001.

[30] Y. Makhlin, G. Schön, and A. Shnirman. Quantum-state engineering with josephson-junction devices. *Reviews of Modern Physics*, 2001.

[31] D. Vion, A. Aassime, A. Cottet, P. Joyez, H. Pothier, C. Urbina, D. Esteve, and M. H. Devoret. Manipulating the quantum state of an electrical circuit. *Science*, 296, May 2002.

[32] Y. Yu, S. Han, X. Chu, S. Chu, and Z. Wang. Coherent temporal oscillations of macroscopic quantum states in a josephson junction. *Science*, 296, May 2002.

[33] T. L. Robertson, B. L. T. Plourde, A. García-Martínez, P. A. Reichardt, B. Chesca, R. Kleiner, Y. Makhlin, G. Schön, A. Shnirman, F. K. Wilhelm, D. J. van Harlingen, and J. Clarke. Superconducting device to isolate, entangle, and read out quantum flux states. submitted to Phys. Rev. Lett.

[34] J. Clarke, T. L. Robertson, B. L. T. Plourde, A. García-Martínez, P. A. Reichardt, D. J. van Harlingen, B. Chesca, R. Kleiner, Y. Makhlin, G. Schön, and A. Shnirman. Quiet readout of superconducting flux states. Notes on INSQUID.